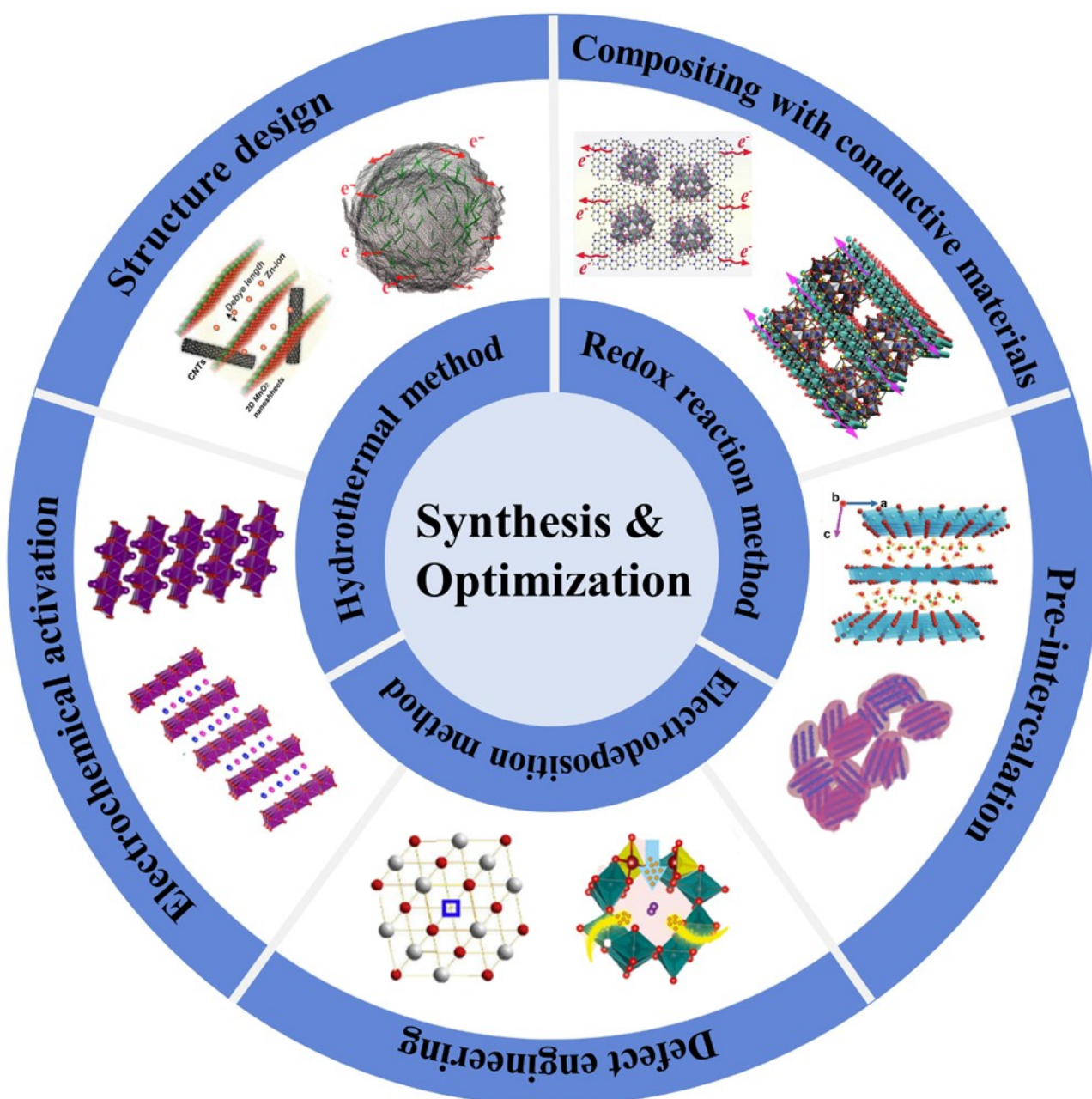


Synthesis and Performance Optimization of Manganese-based Cathode Materials for Zinc-Ion Batteries

Song Wang,^[a] Zhiyuan Sang,^{*[a]} Xinqi Zhao,^[a] Jingdong Guo,^[a] Hao Chen,^[a] and De'an Yang^{*[a]}



Owing to the low cost, high specific capacity and high safety, zinc-ion batteries (ZIBs) have great advantages in replacing lithium-ion batteries to meet future demand for energy storage. Manganese-based cathode materials, benefiting from the abundant reserves, non-toxic, acceptable capacity and long cycle stability, have been widely developed and applied to develop high performance ZIBs. Unfortunately, poor conductivity, Mn^{2+} dissolution and unstable structure hinder it to achieve an ideal electrochemical performance. Thus, an overview of the cathodic performance optimization strategies and the synthesis

is provided. Firstly, the synthesis methods and their influence on the morphology and structure are summarized. Secondly, various strategies of performance optimization, including structure design, compositing with conductive materials, pre-intercalation, defect engineering and electrochemical activation, are categorized and analyzed in detail. Lastly, perspectives on the subsequent performance optimization are proposed. It is expected that this review will be beneficial to future scientific research on tailoring manganese-based cathode materials for ZIBs.

1. Introduction

With the continuous consumption of fossil energy and the intensification of environmental pollution problems, the development of clean, renewable and sustainable energy (such as wind energy, solar energy) is imperative.^[1–3] In order to solve the problems of intermittent and instability of sustainable energy, various energy storage systems have been developed and utilized. Among them, rechargeable batteries with the advantages of low cost, long cycle life, high efficiency and environmental friendliness are considered to be the most feasible options,^[4–6] including lithium-ion battery,^[7–10] sodium-ion battery,^[11–14] potassium-ion battery,^[15–18] lithium-air battery,^[19–22] and so on.

However, the shortage of metal resources has greatly increased the cost of batteries, and the side reactions of organic electrolytes and their flammable and explosive characteristics have increased the safety risks.^[23–26] In recent years, zinc-ion batteries (ZIBs) are expected to be their substitute, due to the following advantages:^[27–31] (1) Abundant storage of zinc in nature, which greatly reduces the cost of ZIBs. (2) Safety and stability, (3) high theoretical capacity of metal zinc (820 mAh g^{-1} or 5854 mAh cm^{-3}) and energy density, (4) low redox potential of zinc (-0.763 V vs. a standard hydrogen electrode [SHE]), which allows the batteries to work in aqueous electrolytes. Therefore, it is crucial for high-performance cathode materials to match the zinc anode of ZIBs.^[27,30,32–35]

Commonly, the cathode materials are focused on manganese-based compounds, vanadium-based compounds,^[36–40] prussian blue analogue,^[41–43] organic materials,^[44–47] etc. Due to high theoretical specific capacity ($\sim 308\text{ mAh g}^{-1}$) and working voltage ($\sim 1.4\text{ V}$), manganese-based cathode materials deliver great competitiveness in the cathode materials of ZIBs. There are still controversies about the energy storage mechanism of manganese-based cathode materials, mainly including: Zn^{2+} insertion/extraction, H^+/Zn^{2+} co-insertion/extraction, chemical conversion reaction, and so on.^[34,35] Unfortunately, many challenges still exist in obtaining high-performance manga-

nese-based cathode materials for ZIBs, as follows: (1) Poor conductivity: it leads to the slow electron transfer kinetics, thus limiting the rate performance of manganese-based cathode. (2) Unstable structure: they suffer from structural damage and large volume change during the repetitive insertion/extraction of ions. (3) Mn^{2+} dissolution: Mn^{2+} can be dissolved in aqueous electrolyte, which may cause the collapse of host structure, thus lead to a capacity fading. These disadvantages seriously affect the actual specific capacity, rate performance and cycle performance.^[32–34,48]

In this review, we focus on the strategies of performance optimization as well including the synthesis methods of manganese-based cathode materials. First, the synthesis methods and their relationship among the preparation-structure-performance are summarized. Second, various strategies of performance optimization are categorized by dividing into five parts: structure design, compositing with conductive materials, pre-intercalation, defect engineering and electrochemical activation (Figure 1). Finally, we make conclusions and perspectives on obtaining high-performance manganese-based cathode

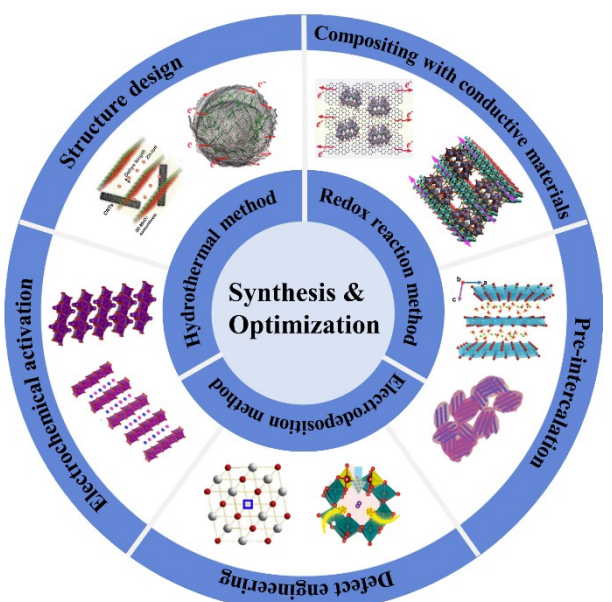


Figure 1. Synthesis methods and strategies of performance optimization for manganese-based cathode materials in ZIBs.

[a] S. Wang, Dr. Z. Sang, X. Zhao, J. Guo, H. Chen, Prof. Dr. D.a. Yang
School of Materials Science and Engineering
Tianjin University
Tianjin, China
E-mail: sangzhiyuan@tju.edu.cn
dayang@tju.edu.cn

materials. On the whole, we hope this review could shed light on the future scientific research on ZIBs.

2. Synthesis of Manganese-based Cathode Materials

For the manganese-based cathode materials, the synthesis methods and synthesis conditions often play a critical role on determining the morphology, structure, and then affect the electrochemical performances. Up to now, several different strategies have been developed to prepare manganese-based cathode materials of ZIBs with various sizes, morphologies (particles, rods, sheets, flowers, etc.), and structures (porous, hollow, etc.), mainly including hydrothermal method, other redox reaction method, electrodeposition method, etc.

2.1. Redox Reaction Method

2.1.1. Hydrothermal Method

Owing to the different connected ways of the basic structural unit $[\text{MnO}_6]$ octahedra, the MnO_2 possesses various crystal structure, including α , β , λ , δ , γ , R and todorokite-type (Figure 2a).^[49] Among them, $\alpha\text{-MnO}_2$ has large $[2\times 2]$ tunnels of $\sim 4.6\text{ \AA}$ for accommodating Zn^{2+} insertion without structural collapse, $\beta\text{-MnO}_2$ exhibits a better cycling stability benefiting

from the 3D tunnel structures, and $\delta\text{-MnO}_2$ with a typical layered structure delivers a layer spacing of 7 \AA for ion diffusion. Notably, hydrothermal method is a feasible strategy for the controlled synthesis of different crystal forms of MnO_2 .

Alfaruqi et al. synthesized highly crystalline $\alpha\text{-MnO}_2$ nanorods by reducing KMnO_4 with H_2SO_4 at 140°C for 8 h.^[50] The $[2\times 2]$ tunnels of the $\alpha\text{-MnO}_2$ structure could withstand the expansion/contraction caused by repeated insertion/extraction of Zn^{2+} (Figure 2b). Similarly, Zhao et al. synthesized $\alpha\text{-MnO}_2$ through the hydrothermal method, and demonstrated the promoting mechanism of Grotthuss proton transport in $[2\times 2]$ tunnels of $\alpha\text{-MnO}_2$.^[51] The O ion on the wall of $[2\times 2]$ tunnels accepts two H^+ after the facile transfer of H^+ via hydrogen bonds. The energy barrier of this Grotthuss proton transport mechanism is significantly lower than that of direct hopping mechanism, which could accelerate the H^+ diffusion in the tunnels of $\alpha\text{-MnO}_2$. (Figure 2c) Therefore, the $\alpha\text{-MnO}_2$ prepared by hydrothermal method with a typical $[2\times 2]$ tunnel structure, shows the fast ion diffusion, and then exhibits an excellent rate performance. Zhang et al. prepared $\beta\text{-MnO}_2$ through a simple hydrothermal reaction at 140°C for 12 h.^[52] In initial discharge, the $\beta\text{-MnO}_2$ transforms into the $\text{Zn}_x\text{MnO}_2\cdot n\text{H}_2\text{O}$ with a layered structure for Zn^{2+} insertion/extraction (Figure 2d), and the $\text{Zn}/\beta\text{-MnO}_2$ battery shows a long-term cycling stability with 94% capacity retention over 2000 cycles at a high current density of 6.5 C (Figure 2e). Liao et al. synthesized $\beta\text{-MnO}_2$ with a preferred crystal orientation through the hydrothermal reaction between MnSO_4 and APS at 140°C for 8 h, which delivers an enhanced electrochemical performance.^[53] In addition, Guo



Song Wang received his bachelor's degree in the Department of Materials Science and Engineering, Tianjin University in 2019. He is currently a M.D candidate in the Department of Materials Science and Engineering at Tianjin University. His research focuses on the cathode materials of zinc-ion battery.



Zhiyuan Sang received his Ph.D. degree from the School of Materials Science and Engineering in Tianjin University in 2020, and then worked as an assistant research fellow. His research focuses on nanomaterials for energy storage and conversion, including metal-ion batteries and electrocatalysis.



Xinqi Zhao is currently a Ph.D candidate in the Department of Materials Science and Engineering at Tianjin University. She received her bachelor's degree in Chemical Materials and Engineering from Guizhou University in 2018. Her research focuses on development of functional materials for high performance zinc-ion batteries and lithium-sulfur batteries.



Jingdong Guo is currently pursuing his Ph.D. degree in the Department of Materials Science and Engineering at Tianjin University. He received his bachelor's degree in the Department of Materials Science and Engineering at University of Jinan in 2015. His research focuses on development of vanadium based oxide for high performance zinc-ion battery.



Hao Chen is currently a M.D candidate in the Department of Materials Science and Engineering at Tianjin University. He received his bachelor's degree in the Department of Materials Science and Engineering at Tianjin University in 2020. His research focuses on development of functional materials for high performance zinc-ion battery.



De'an Yang received his Ph.D. degree under the supervision of Prof. Tingxian Xu at School of Materials Science and Engineering, Tianjin University. He is currently a Prof. at Tianjin University. His research focuses on functional ceramics.

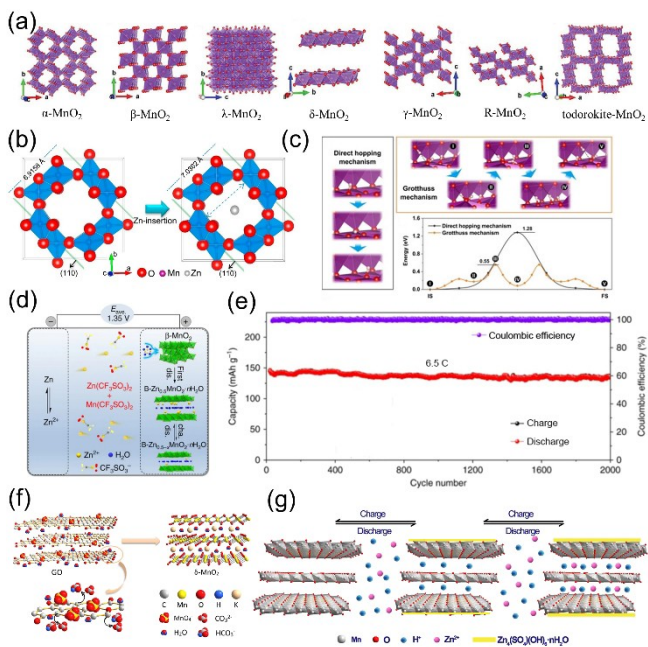


Figure 2. a) Various crystal structures of MnO_2 . Adapted with permission from Ref. [49]. Copyright (2019) Royal Society of Chemistry. b) Schematic illustration of Zn^{2+} insertion into the tunnel of $\alpha\text{-MnO}_2$. Adapted with permission from Ref. [50]. Copyright (2015) Elsevier S. A. c) H^+ ion migration pathway and corresponding energy barriers of direct hopping mechanism and Grothuss proton transport mechanism in $[2 \times 2]$ tunnels of $\alpha\text{-MnO}_2$. Adapted with permission from Ref. [51]. Copyright (2020) Wiley-VCH. d) Schematic illustration of $\text{Zn}/\beta\text{-MnO}_2$ battery. e) cycle performance of $\text{Zn}/\beta\text{-MnO}_2$ battery. Adapted with permission from Ref. [52]. Copyright (2017) Springer Nature. f) Illustration of the formation of $\delta\text{-MnO}_2$. g) schematic illustration of charge-discharge process with ions insertion/extraction. Adapted with permission from Ref. [54]. Copyright (2019) Elsevier.

et al. prepared ultrathin $\delta\text{-MnO}_2$ nanosheets using graphene oxide (GO) as the reductant and self-sacrificing template (Figure 2f).^[54] The stable layered structure could allow the H^+ and Zn^{2+} co-insertion/extraction (Figure 2g), which makes an explanation for the discharge capacity of 133 mAh g^{-1} after 100 cycles at 0.1 A g^{-1} . Recently, we also synthesized $\delta\text{-MnO}_2$ through the direct hydrothermal of KMnO_4 at 160°C for 12 h.^[55]

α , β , $\delta\text{-MnO}_2$ with the typical tunnel structure or layered structure are the main form of MnO_2 -based cathode in ZIBs. In contrast, limited by the specific capacity, there are fewer reports of other crystal types, such as $\lambda\text{-MnO}_2$,^[56] $\gamma\text{-MnO}_2$,^[57] etc. In short, diverse crystal types lead to the differences in electrochemical performance and energy storage mechanism. Hydrothermal method can synthesize different crystal forms of MnO_2 by adjusting specific parameters, which provides a reference for the preparation of MnO_2 with the specific crystal forms.

In addition, hydrothermal method has been widely used to synthesize nano-sized materials with various sizes and different morphologies. Figure 3(a-g) lists the different morphologies of MnO_2 , including nanoparticles,^[58] nanowires,^[59] nanorods,^[60] nanofibers,^[61] nanoflakes,^[62] urchin-like microspheres with nanorods,^[63] and nanospheres,^[64] which were prepared through hydrothermal methods by changing the synthesis parameters (raw materials, temperature, time, etc.). First, these nano-sized

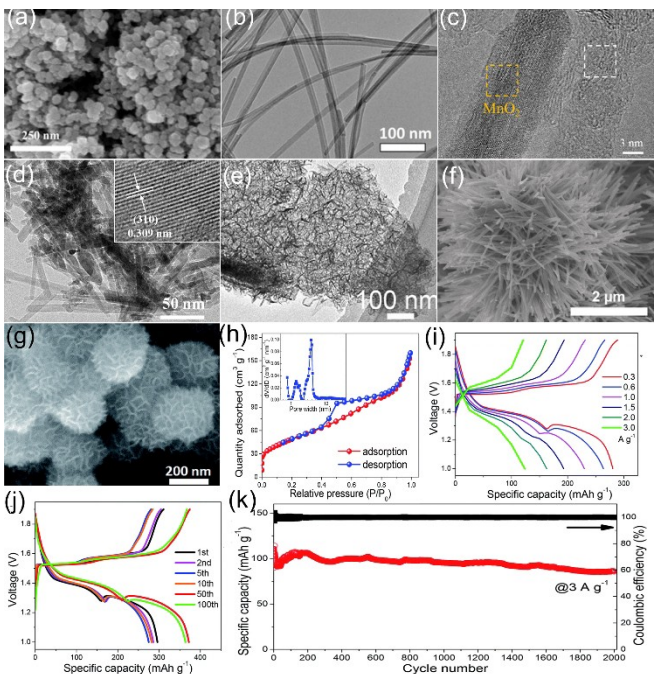


Figure 3. Different morphologies of MnO_2 : a) nanoparticles. Adapted with permission from Ref. [58]. Copyright (2017) Elsevier. b) Nanowires. Adapted with permission from Ref. [59]. Copyright (2020) American Chemical Society. c) Nanorods. Adapted with permission from Ref. [60]. Copyright (2020) Elsevier. d) Nanofibers. Adapted with permission from Ref. [61]. Copyright (2019) Elsevier. e) Nanoflakes. Adapted with permission from Ref. [62]. Copyright (2020) Elsevier. f) Urchin-like microspheres with nanorods. Adapted with permission from Ref. [63]. Copyright (2020) Springer. g) Nanospheres, h) Nitrogen adsorption-desorption isotherms and pore-size distributions (inset) of the MnO_2 nanospheres, i) GCD curves at different current densities of 0.3 to 3 A g^{-1} , j) GCD curves of different cycles at 0.3 A g^{-1} , k) cycle performance at 3 A g^{-1} of MnO_2 nanospheres cathode. Adapted with permission from Ref. [64]. Copyright (2019) Royal Society of Chemistry.

and porous structures greatly provide sufficient active sites for energy storage. Second, these structures shorten the ion/electron transmission path, accelerating the kinetics process. Finally, they provide the enough room to tailor the volume changes during the repeated Zn^{2+} insertion/extraction, ensuring the stability of the structures. For instance, the MnO_2 nanospheres deliver a large specific surface area ($178 \text{ m}^2 \text{ g}^{-1}$) and a total pore volume of $0.25 \text{ cm}^3 \text{ g}^{-1}$ (Figure 3h).^[64] Therefore, the battery achieves a high reversible capacity of 275 mAh g^{-1} at 0.3 A g^{-1} , a high retained capacity of 121 mAh g^{-1} at 3 A g^{-1} (Figure 3i), and an excellent cycle stability at the current density of 0.3 and 3 A g^{-1} (Figure 3k).

Besides MnO_2 , hydrothermal method is also a convenient way to synthesize other manganese-based compounds, including MnO ,^[65] Mn_3O_4 ,^[66,67] ZnMn_2O_4 ,^[68,69] etc. For instance, Zhu et al. putted KMnO_4 in the hydrothermal reaction at 140°C to synthesize Mn_3O_4 .^[66] Reaction time of 24 h leads to a compact and uniform Mn_3O_4 nanoflowers composed of ultrathin nanosheets. And the Mn_3O_4 cathode delivers a high specific capacity of 296 mAh g^{-1} at 0.1 A g^{-1} and there is no capacity fading after 500 cycles at 0.5 A g^{-1} .

In summary, hydrothermal synthesis is an efficient method to prepare various manganese-based nanocomposites with different sizes, morphologies and crystal structure. And the nano-sized manganese-based cathode materials share the advantages of fast transfer of ions and electrons as well as the sufficient contact area with the electrolyte, which will greatly improve the electrochemical performance in ZIBs.

2.1.2. Other Redox Reaction Method

Manganese itself has different valence states (Mn^{2+} , Mn^{3+} , Mn^{4+} , and Mn^{7+}), which provides the possibility of preparing different manganese-based compounds by redox reaction. As shown in Figure 4(a), Lee et al. used the reduction reaction of $KMnO_4$ to grow MnO_2 on the surface of flexible graphene film (FSM@FGF).^[70] After reacting at 80°C for 60 min, the MnO_2 needles with the size of 101.3–118.1 nm are well anchored on the FGF surface (Figure 4b). The free-standing FSM@FGF-60 cathode delivers the fast Zn^{2+} diffusion and electron transfer, leading to a high capacity of 301.0 $mAhg^{-1}$ at 1 Ag^{-1} and a capacity retention of 82.7% after 300 cycles (Figure 4c). As shown in Figure 4(d), Zang et al. prepared MnO_x by limitedly reducing MnO_2 with hydrazine vapor.^[71] The valence state of Mn decreases with the increase of the amount of hydrazine hydrate (Figure 4e). Compared to MnO_2 , MnO_x with a lower valence state of Mn shows the more rapid transfer of charges and the superior structural stability. Unlike this, Lu et al. directly synthesized MnO_2 nanosheets through the redox process of Mn^{2+} using hydrogen peroxide as the oxidizing agent.^[72] The MnO_2 nanosheets have a typical layered structure with a lot of wrinkles, which provide a large number of active sites for Zn^{2+} insertion.

Additionally, redox reaction method is also helpful for synthesizing transition metals-doped MnO_2 samples. Xu et al. added $KMnO_4$ to the mixed solution of $Mn(CH_3COO)_2$ and $Fe(NO_3)_3$ to obtain Fe-doped MnO_2 (Figure 5a). The process is achieved by stirring and annealing, and the prepared Fe-doped

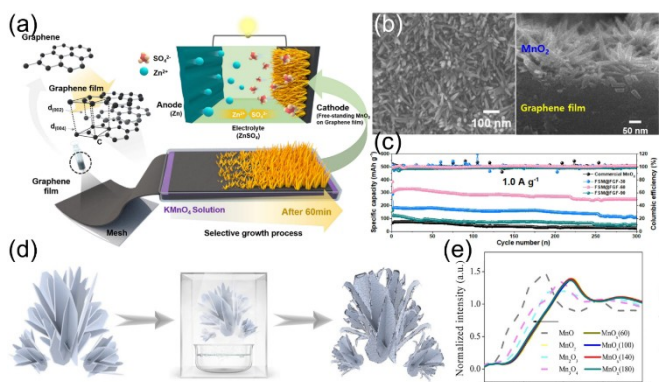


Figure 4. a) Schematic diagram of the synthesis of FSM@FGF, b) SEM of FSM@FGF-60, c) cycle performance of FSM@FGF at 1.0 Ag^{-1} . Adapted with permission from Ref. [70]. Copyright (2021) Elsevier. d) Schematic reaction of synthesizing MnO_x , e) Mn K-edge XANES spectra of MnO_x . Adapted with permission from Ref. [71]. Copyright (2021) Elsevier.

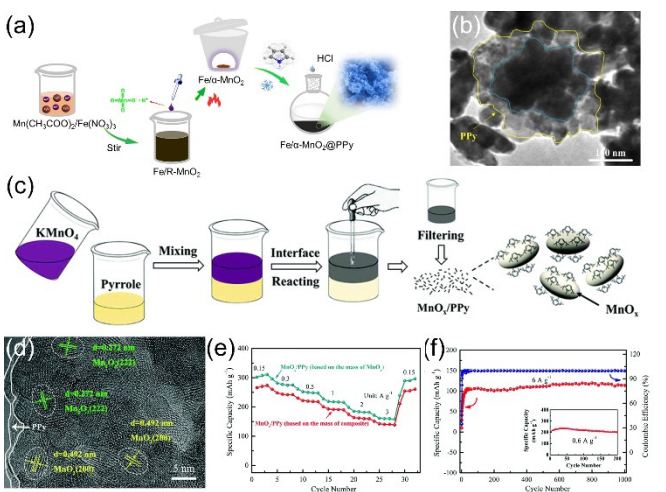


Figure 5. a) Preparation schematic diagram of $Fe/\alpha\text{-}MnO_2@PPy$, b) TEM images of $Fe/\alpha\text{-}MnO_2@PPy$. Adapted with permission from Ref. [73]. Copyright (2021) Elsevier. c) Schematic illustration of MnO_x/PPy , d) SEM image of MnO_x/PPy , e) rate performance and f) cycle performance of MnO_x/PPy . Adapted with permission from Ref. [76]. Copyright (2020) Royal Society of Chemistry.

MnO_2 presents the morphology of nanoparticles without other impurities (Figure 5b). Similarly, Alfaruqi et al. prepared V-doped MnO_2 spheres by introducing V_2O_5 into the precursor solution of $KMnO_4$ and $Mn(CH_3COO)_2$.^[74] The entire synthesis process is carried out at ambient temperature.

Also, redox reaction method has the unique advantages in the preparation of manganese-based composite materials.^[75] Li et al. synthesized MnO_x/PPy composites through organic/inorganic interface redox reaction using pyrrole and $KMnO_4$ as the precursor (Figure 5c).^[76] The chemical polymerization of pyrrole and the reduction of MnO_4^- occurred simultaneously, facilitating the formation of MnO_x/PPy . As shown in Figure 5(d), the synthesized MnO_x nanoparticles possessed a typical size of 11 nm covered by PPy nanolayers. The cathode suggests a high specific capacity of 159.9 $mAhg^{-1}$ (based on the mass of MnO_x) at 3 Ag^{-1} (Figure 5e) and remains a capacity of 113.7 $mAhg^{-1}$ after 1000 cycles at an extremely high current density of 6 Ag^{-1} (Figure 5f).

2.2. Electrodeposition Method

Electrodeposition works by depositing solvated ionic species onto a conductive substrate by applying an external potential or current. This method has the following characteristics: (1) Excellent conductivity: The conductive substrates are carbon materials in most cases, which can effectively improve the overall conductivity of cathode materials. (2) Porous structure: The interconnected nanostructures of manganese-based compounds form a highly porous structure. (3) Self-supporting (binder-free): The manganese-based compounds can be deposited on the conductive substrates, which is directly used as the cathode without any additives (such as binder).

In ZIBs, electrodeposited manganese-based compounds have a nanocrystalline structure, usually in the form of interconnected nanosheets.^[30,77] Sun et al. deposited MnO₂ on the surface of the carbon fiber paper (CFP) through a potential-static method (Figure 6a).^[78] The MnO₂ is composed of the interconnected nanoflakes and forms a highly porous structure (Figure 6b). On the one hand, MnO₂ nanoflakes provide abundant electrode/electrolyte contact interfaces and active sites for energy storage. On the other hand, the morphology of nanoflakes reduces the ions diffusion path and the porous structure allow the volume changes during ions insertion/extraction. As a result, the battery displays a specific discharge capacity of 260 mAh g⁻¹ at 1.3 C and an excellent cycle stability over 10000 cycles at 6.5 C (Figure 6c). And the reaction mechanism of H⁺ and Zn²⁺ co-insertion/extraction is investigated by galvanostatic intermittent titration technique (GITT) and electrochemical impedance spectroscopy (EIS). Specifically, due to the much smaller size of H⁺ and Zn²⁺, the insertion of Zn²⁺ happens after the H⁺-insertion. (Figure 6d, e) The ex-situ XRD patterns at different states also confirm this. (Figure 6f) Notably, MnO₂ prepared by electrodeposition method is mostly the delta phase, which delivers the typical H⁺ and Zn²⁺ co-insertion/extraction and shows a fast reaction kinetics.

Electrodeposition method is also a simple method to obtain the metals-doped manganese-based cathode materials. Kataoka et al. added CoSO₄ to the electrolyte to prepare cobalt-doped layered MnO₂.^[79] Affected by cobalt doping, Co-MnO₂ shows a pleated morphology, suggesting an increased surface area (Figure 6g). Benefiting from N-doped carbon cloth substrate and Co-doped MnO₂, the Zn/Co-MnO₂/N-CC generates a discharge capacity of 280 mAh g⁻¹ at 1.2 A g⁻¹ after 600 cycles and a remained capacity of 30 mAh g⁻¹ at an extremely high current density of 10.5 A g⁻¹ (Figure 6h, i). To shorten the

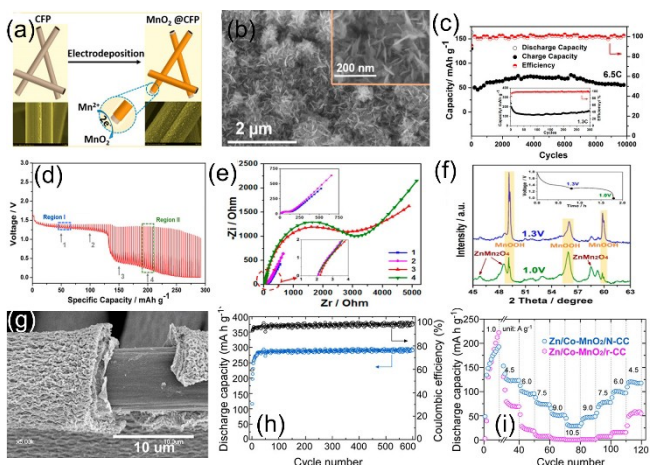


Figure 6. a) Schematic illustration of synthesis process MnO₂@CFP, b) SEM image of MnO₂@CFP, c) cycle performance of MnO₂@CFP cathode, d) GITT profiles, e) nyquist plots at different depth of discharge, f) ex-situ XRD patterns at depth of discharge at 1.3 V and 1.0 V of the MnO₂@CFP cathode. Adapted with permission from Ref. [78]. Copyright (2017) American Chemical Society. g) SEM images of Co-MnO₂ films, h) cycle performance and i) rate performance of Zn/Co-MnO₂/N-CC battery. Adapted with permission from Ref. [79]. Copyright (2020) American Chemical Society.

synthesis time, Dhiman et al. adopted a novel pulse electrodeposition method to prepare Mn₃O₄ onto carbon paper at a current of 4.7 mA with a 0.25 s ON cycle and a 0.5 s OFF cycle for a total of 2400 cycles.^[80] The pulse electrodeposition method exhibits huge advantages on controlling the thickness of the deposited products, thus the obtained Mn₃O₄ nanosheets is only 1–2 μm, greatly shortening the ion/electron transmission path and the battery delivers a discharge capacity of 143 mAh g⁻¹ at 2.4 A g⁻¹.

In addition, the electrodeposition method commonly adopted to prepare flexible electrodes, which is expected to meet the needs of flexible energy storage devices. Wang et al. prepared a MnO₂@CNT fiber-like cathode by electrodeposition method (Figure 7a).^[81] When it was assembled into a cable-type flexible battery, the battery could be twisted or bent without sacrificing the electrochemical performance, even after 100 bending cycles (Figure 7b, c). Zeng et al. synthesized MnO₂@PEDOT cathode through the electrodeposition method and assembled a flexible quasi-solid-state rechargeable Zn-MnO₂ battery (Figure 7d).^[82] Due to the flexible cathode, the battery could work under the bending conditions (Figure 7e) and be applied to the flexible and wearable electronics (Figure 7f). Wang et al. electrodeposited PPy-coated MnO₂ onto stainless steel (SS) yarn (Figure 7g),^[83] and the assembled wire-shaped battery displays the excellent mechanical flexibility, which could be bent to different angles without reducing electrochemical performance (Figure 7h, i).

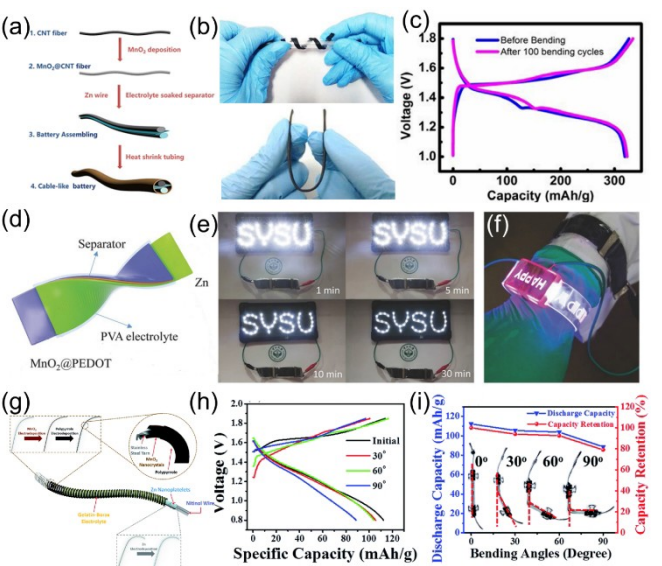


Figure 7. a) Schematic of preparation process of Zn-MnO₂ cable battery, b) flexibility of the Zn-MnO₂ cable battery, c) GCD curves before and after 100 bending cycles. Adapted with permission from Ref. [81]. Copyright (2018) American Chemical Society. d) Schematic illustration of flexible Zn-MnO₂@PEDOT battery, e) photographs of light-emitting diodes and f) a watch powered by Zn-MnO₂@PEDOT batteries. Adapted with permission from Ref. [82]. Copyright (2017) Wiley-VCH. g) Schematic diagram of Zn/NT-MnO₂/PPy@SS wire-shaped battery, h) GCD curves and i) discharge capacity of the bent wire-shaped battery at different angles. Adapted with permission from Ref. [83]. Copyright (2018) Royal Society of Chemistry.

To sum up, different methods will affect the structure (tunnel structure, layered structure, etc.) of manganese-based cathode materials, which in turn affects the ion-transfer mechanism and electrochemical performance. Also, the synthesis methods often play a crucial role on deciding the morphology and structure. Briefly, As a typical redox reaction method, hydrothermal method helps to control the crystal form, morphology, and structure of manganese-based cathode materials. And redox reaction methods are the viable option to achieve the doping. Electrodeposition method has the significant advantages in self-supporting and flexible electrodes. Different methods will affect the structure (tunnel structure, layered structure, etc.) of manganese-based cathode materials, which in turn affects the ion-transfer mechanism and electrochemical performance. Besides the above methods, sol-gel method,^[84] microemulsion method,^[85,86] molten salt method,^[87] thermal decomposition method,^[88] co-precipitation method,^[89] etc. have also been reported. These methods provide guidance for the synthesis of high-performance manganese-based cathode materials with different crystal forms, morphologies and structures, which are detailedly listed in Table 1.

3. Strategies of Performance Optimization

3.1. Structure Design

3.1.1. 0D–3D Nanostructure

According to dimensions, manganese-based cathode materials can be divided into four categories: (1) 0D: Nanoparticles; (2) 1D: Nanowires, nanotubes and nanorods; (3) 2D: Nanosheets and nanoplates; (4) 3D: Assembled structures such as nanospheres and nanoflowers. Due to the size effect, nanostructures are preferred in the performance optimization of manganese-based cathode materials. They have the following advantages: (1) High electrode/electrolyte contact area, providing a large number of active sites for energy storage and promoting the ion diffusion at interfaces. (2) Short transmission path for ions and electrons, improving the electrochemical kinetic process. (3) Better adapt to the volume change of ions insertion/extraction, improving the cycle stability.

Benefiting from the large specific surface area and short diffusion distance, nano-structured manganese-based cathode materials often suggest high reversible capacities and excellent rate performances. Jiang et al. prepared the Mn₃O₄ nanodots with an average size of 6.0 nm (Figure 8a), through refluxing and solvothermal treatment.^[90] Due to the size effect of nanodots, when tested as cathode for ZIBs (Figure 8b), the Mn₃O₄ cathode possesses a large Zn²⁺ diffusion coefficient of $2.4 \times 10^{-10} \text{ cm}^2 \text{s}^{-1}$ (Figure 8c) and a rather low charge transfer resistance (Figure 8d). In addition, the capacity contribution

Table 1. Synthesis methods of various manganese-based cathode materials.

Synthesis methods	Manganese-based cathode material	Morphology	Size	Capacity [mAh g ⁻¹]/current density [A g ⁻¹]	Ref.
hydrothermal method	$\alpha\text{-MnO}_2$	nanorods	20 nm in width, 200 nm in length	233/0.083	[50]
hydrothermal method	$\beta\text{-MnO}_2$	nanorods	150 nm in diameter	258/0.2	[52]
hydrothermal method	$\delta\text{-MnO}_2$	nanosheets	2–4 nm in thickness	133/0.1	[54]
hydrothermal method	$\alpha\text{-MnO}_2@\text{C}$	nanoparticles	20 nm in size	272/0.066	[58]
hydrothermal method	D-MnO ₂	nanowires	10 nm in diameter	290/0.3	[59]
hydrothermal method	$\Gamma\text{-MnO}_2@\text{graphene}$	nanorods	10–20 nm in diameter	301/0.5	[60]
hydrothermal method	$\alpha\text{-MnO}_2@\text{CNT}$	nanofibers	8 nm in diameter	296/0.2	[61]
hydrothermal method	N-CNS@MnO ₂	nanoflakes	200–300 nm in thickness	303.7/0.2	[62]
hydrothermal method	$\alpha\text{-MnO}_2$	urchin microspheres with nanowires	4–10 μm in diameter	308/0.1	[63]
hydrothermal method	$\alpha\text{-MnO}_2$	nanospheres	200 nm in diameter	275/0.3	[64]
other redox reaction method	FSM@FGF	needle-shaped particles	103.7–110.2 nm in size	440/0.1	[70]
other redox reaction method	MnO _x	nanoflowers	150 nm in diameter	487.6/0.2	[71]
other redox reaction method	Fe/MnO ₂ @PPy	nanoparticles	30–80 nm in size	270/0.1	[73]
other redox reaction method	V-doped MnO ₂	spherical particles	50 nm in diameter	266/0.066	[74]
other redox reaction method	MnO _x /PPy	nanoparticles	11 nm in size	302/0.15	[76]
electrodeposition method	MnO ₂ @CFP	nanoflakes	10 nm in thickness	290/0.1	[78]
electrodeposition method	Co-doped MnO ₂	thin film	–	288/0.3	[79]
electrodeposition method	Mn ₃ O ₄	flake-like islands	1–2 μm in thickness	328/0.3	[80]
electrodeposition method	MnO ₂ @CNT	fibers	100–120 μm in length	322/0.1	[81]
electrodeposition method	MnO ₂ @PEDOT	film	–	366.6/0.74	[82]
electrodeposition method	PPy coated MnO ₂	nancrystallites	20 nm in crystal size	143.2/0.3	[83]
sol-gel method	K _{0.41} MnO ₂ ·0.5H ₂ O	nanosheets	50 nm in thickness	425/0.175	[84]
microemulsion method	$\alpha\text{-MnO}_2$	nanorods	12 nm in diameter	210/0.5	[85]
molten salt method	MnO ₂ /Mn ₂ O ₃	nanobelts/nanoparticles	–	322.1/0.2	[87]
thermal decomposition method	$\delta\text{-MnO}_2$	flake-like particles	200 nm in diameter	252/0.083	[88]
co-precipitation method	$\alpha\text{-MnO}_2$	nanorods	10 nm in diameter, 50–120 nm in length	665/0.1	[89]

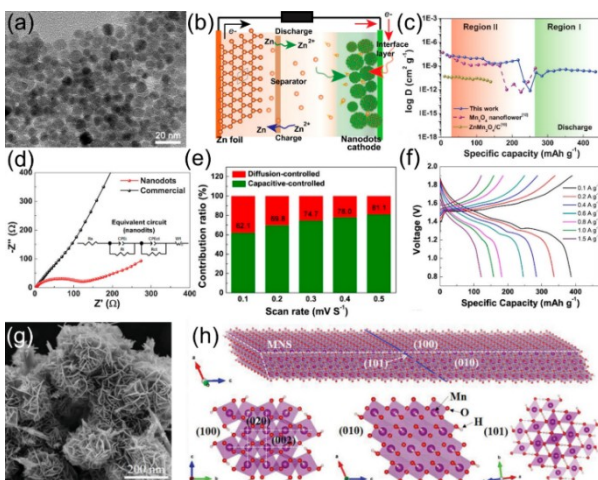


Figure 8. a) TEM image of Mn_3O_4 nanodots, b) schematic representation of Zn^{2+} transport in $\text{Zn}-\text{Mn}_3\text{O}_4$ battery, c) Zn^{2+} diffusion coefficient, d) EIS of $\text{Zn}-\text{Mn}_3\text{O}_4$ battery, e) Contribution ratio of capacities at different scan rates, f) GCD curves at different current densities. Adapted with permission from Ref. [90]. Copyright (2019) American Chemical Society. g) SEM image of MnO_2 nanosheets, h) schematic illustration of MnO_2 polyhedral models. Adapted with permission from Ref. [91]. Copyright (2019) Wiley-VCH.

mainly comes from the capacitive process (Figure 8e), which is favorable for the fast kinetics. As a result, the cathode achieves a high capacity of 386.7 mAh g^{-1} at 0.1 A g^{-1} and a superior rate performance of 121.6 mAh g^{-1} at 1.5 A g^{-1} (Figure 8f). Zhao et al. synthesized MnO_2 nanosheets through one-step hydrothermal method (Figure 8g).^[91] The MnO_2 nanosheets with a surface area of $120 \text{ m}^2 \text{ g}^{-1}$ and a thickness of 2.5 nm , not only provides the sufficient active sites, but also shorten the ion transmission path. In particular, the (100) plane of MnO_2 presents large exposed areas of 1×1 tunnel for the transmission of H^+ and Zn^{2+} (Figure 8h), thus endowing a super rate performance of 115.1 mAh g^{-1} at a high current rate of 10 C .

Besides promoting the ion/electron transfer kinetics, nanostructures also have unique advantages in cycle stability. Wang et al. prepared single-atomic layer MnO_2 nanosheets with a thickness of 1 nm (Figure 9a, b) through the exfoliation process.^[92] Compared with the tip-effect caused by sharp corners and irregular morphology of bulk MnO_2 , the smooth surface formed by the MnO_2 nanosheets could significantly reduce the concentration gradient in the electrolyte and promote the uniform stripping/plating (Figure 9c), thus endowing a superior cycle stability over 600 cycles (Figure 9d). Ren et al. also constructed the inverse opal MnO_2 ultrathin nanosheets (IO- MnO_2) with the thickness of approximately 1 nm (Figure 9e).^[93] In MnO_2 inverse opal structure, the hollow parts encompassed by nanosheets adapt to the volume expansion of ion insertion and avoid structural collapse. As a result, the IO- MnO_2 cathode could keep a capacity of 121 mAh g^{-1} even after 5000 long-term cycles at 2 A g^{-1} (Figure 9f).

In recent years, 3D assembly structures based on nanostructures have also been reported.^[61, 64, 94–96] For example, Shi et al. synthesized a 3D micro-flowers-like structure of MnO_2 nanowires (Figure 10a) through spray drying technology.^[95] The

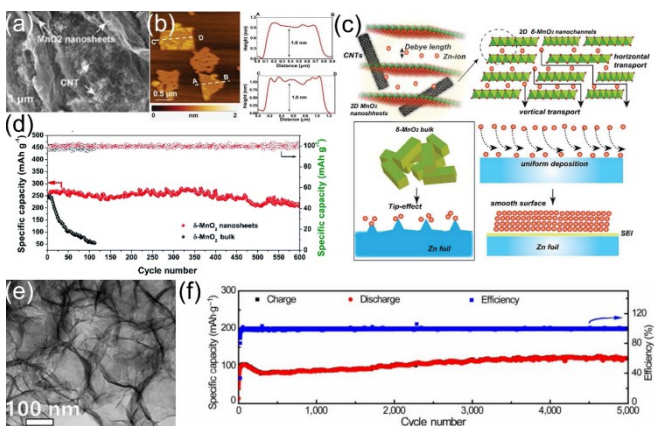


Figure 9. a) SEM image and b) AFM image of MnO_2 nanosheets, c) schematic illustration of Zn^{2+} transport process in MnO_2 nanosheets and $\delta\text{-MnO}_2$ bulk, d) cycle performance of MnO_2 nanosheets and $\delta\text{-MnO}_2$ bulk cathode at 0.1 A g^{-1} . Adapted with permission from Ref. [92]. Copyright (2019) Royal Society of Chemistry. e) TEM image of IO- MnO_2 , f) cycle performance of IO- MnO_2 cathode at 2 A g^{-1} . Adapted with permission from Ref. [93]. Copyright (2019) Springer.

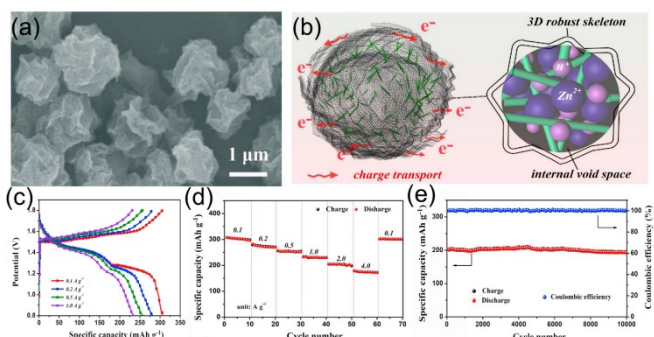


Figure 10. a) SEM image of 3D micro-flowers-like MnO_2 , b) schematic diagram of 3D micro-flowers-like structure confined MnO_2 nanowires. c) GCD curves at different current densities, d) rate performance and e) cycle performance at 2 A g^{-1} of 3D micro-flowers-like MnO_2 cathode. Adapted with permission from Ref. [73]. Copyright (2020) Elsevier.

3D structure provides abundant reaction sites, convenient ion/electron diffusion channels and enough room to alleviate the volume expansion (Figure 10b). Thus, the battery delivers a high capacity of 306.8 mAh g^{-1} at 0.1 A g^{-1} (Figure 10c) and a superior rate capacity of 180.2 mAh g^{-1} at 4 A g^{-1} (Figure 10d). What's more, an ultralong-cycle stability of $\sim 97.5\%$ retention even after 10000 cycles is achieved (Figure 10e).

There is no doubt that nanostructures have unique advantages in the performance optimization of manganese-based cathode materials due to the typical size effect. Based on the characteristics of the nanostructures, such as high specific surface, fine electron/ion transport channels, etc. the reasonable nanostructure or assembly structures design is a feasible strategy for performance optimization.

3.1.2. Porous and Hollow Structure

The porous or hollow structure provides more active sites for energy storage and channels for ion diffusion. At the same time, the pores alleviate the volume change caused by repeated ion insertion/extraction, which is beneficial to the structural stability. Up to now, porous or hollow structure has been widely applied to improve the electrochemical performance of manganese-based cathode materials in ZIBs.^[66,97–102] Feng et al. prepared mesoporous Mn_2O_3 (MMO) with controllable pore size and large specific surface areas.^[97] For the MMO with pore size of 3.2 nm (MMO-3.2), it shows the morphology of nanoparticles with a diameter of 5 nm (Figure 11a) and the specific surface area is $260 \text{ m}^2 \text{ g}^{-1}$ (Figure 11b, c). The porous structure exposes a large number of active sites and alleviates the volume expansion of Zn^{2+} insertion. Benefiting from this, the mesoporous MMO-3.2 cathode delivers a high capacity of 292 mAh g^{-1} at 0.2 A g^{-1} , an excellent rate performance (162 mAh g^{-1} retains at 3.08 A g^{-1}) and cycle stability over 3000 cycles at 3.08 A g^{-1} (Figure 11d, e).

The hollow structure can be regarded as a special porous structure. Guo et al. prepared the hollow MnO_2 nanospheres with a specific surface area of $200 \text{ m}^2 \text{ g}^{-1}$.^[98] The hollow MnO_2 shell is around 15 nm thick (Figure 11f), which extremely shorten the Zn^{2+} diffusion path, and avoid structural collapse caused by volume expansion during the ion insertion. Therefore, the hollow MnO_2 cathode suggests a high specific capacity up to 405 mAh g^{-1} at 0.5 C (Figure 11g) and the discharge capacity is stabilized at 305 mAh g^{-1} after 100 cycles at 1 C (Figure 11h).

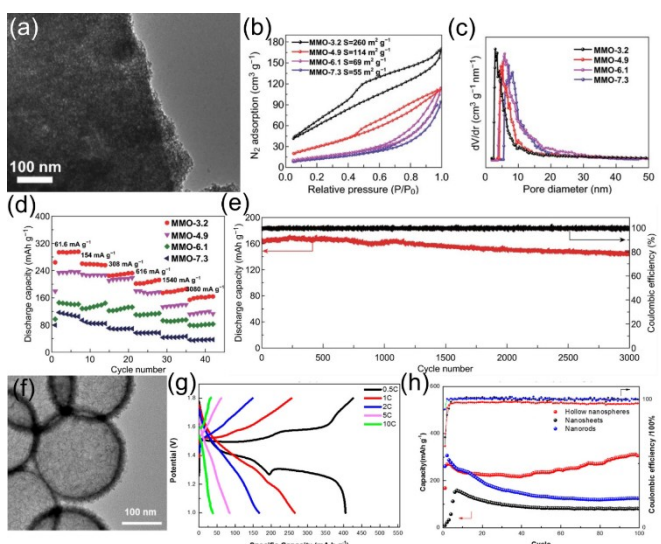


Figure 11. a) TEM image of MMO-3.2, b) nitrogen sorption isotherms and c) pore-size distribution curves of MMO, d) rate performance and e) cycle performance at 3.08 A g^{-1} MMO cathode. Adapted with permission from Ref. [97]. Copyright (2020) Springer. (f) TEM image of hollow MnO_2 nanospheres, (g) GCD curves at different current densities, (h) cycle performance of hollow MnO_2 cathode. Adapted with permission from Ref. [98]. Copyright (2018) The authors.

To summarize, the structures affect the specific surface area, ion/electronic diffusion distance, etc. directly, which in turn affect the specific capacity, rate performance and cycle stability of manganese-based cathode. Anyway, Reasonable structure design is a viable option to further improve the performance of manganese-based cathode in ZIBs.

3.2. Compositing with Conductive Materials

Structure design is difficult to solve the problem of poor conductivity of the manganese-based cathode materials, and the structural stability of the materials still needs to be improved. Compositing with conductive materials (carbon materials, conductive polymers, etc.) is a commonly used strategy to improve the conductivity and structural stability.

3.2.1. Inorganic Carbon Materials

In recent years, various studies have reported the application of carbon materials in manganese-based cathode materials.^[61,62,65,68,99,103–107] Carbon materials with high conductivity, including porous carbon, graphene, etc., are widely used in composite materials, which can serve as substrate, network, coating, and so on. The carbon materials play a vital role in the electron/ion transport and structural stability of manganese-based cathode materials. With the development of different types and sizes of carbon materials, they have shown great potential in manganese-based cathode materials.

Carbon materials are good substrates for in-situ growth of manganese-based compounds. Yang et al. prepared ZnMn_2O_4 nanoparticles anchored on the porous carbon polyhedrons (ZMO@PCPs) (Figure 12a).^[68] The porous carbon as the substrate, acts as the “highways” for electronic transmission (Figure 12b), thus leading to the fast electron transfer kinetics. Therefore, the MO@PCPs cathode delivers a prominent rate capacity of 88.7 mAh g^{-1} at 4 A g^{-1} (Figure 12c).

Carbon network with excellent mechanical stability not only accelerates the electron transmission, but also guarantees the structural stability due to its porous structure. Fu et al. prepared onion-like N-doped carbon composites with MnO_x nanorods ($\text{MnO}_x@\text{N-C}$) (Figure 12d),^[99] in which the carbon conductive network would significantly reduce the charge transfer resistance (Figure 12e), improving the overall conductivity. In addition, the porous structure of the carbon network adapts to the volume expansion of ions insertion. As a result, the battery delivers a superior rate performance of 100 mAh g^{-1} at 2 A g^{-1} and a long-term cycle performance up to 1600 cycles at the current densities of 1 and 2 A g^{-1} (Figure 12f).

Coating is an important form of carbon materials in composite materials. The carbon coating promotes electron/ion transfer, and plays a key role in inhibiting the dissolution of Mn^{2+} . Wu et al. obtained $\alpha\text{-MnO}_2/\text{graphene scrolls}$ by uniformly coating graphene scrolls on MnO_2 nanowires.^[107] The graphene coating effectively alleviated the dissolution of Mn^{2+} , which greatly increased the structural stability during cycling. There-

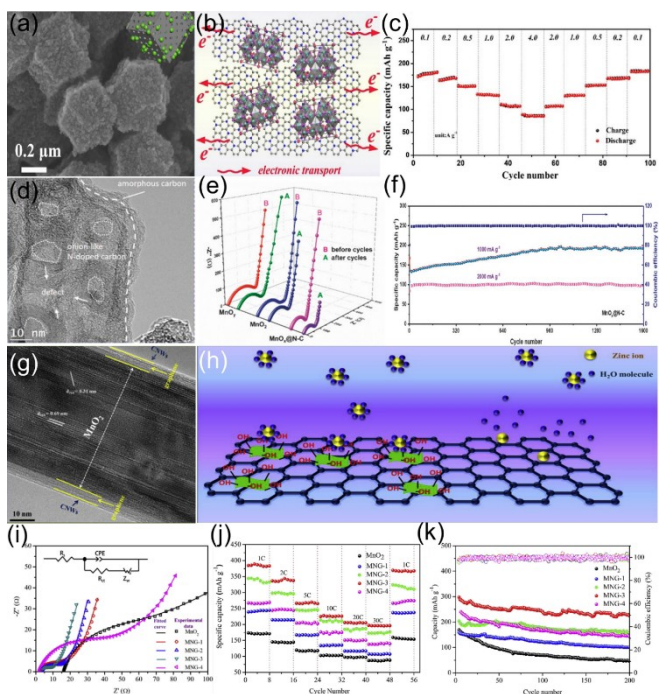


Figure 12. a) SEM image of ZMO@PCPs, b) schematic diagram of electronic transport in ZMO@PCPs, c) rate performance of ZMO@PCPs cathode. Adapted with permission from Ref. [68]. Copyright (2020) Elsevier. d) TEM image of MnO_x@N-C composite, e) EIS and f) cycle performance of MnO_x@N-C cathode at 1 and 2 A g⁻¹. Adapted with permission from Ref. [99]. Copyright (2018) Wiley-VCH. g) HRTEM image of MNG, h) schematic diagram of hydrated Zn²⁺ desolvation at MNG surface, i) EIS of MNG cathode, j) rate performance and k) cycle performance at 5 C of MNG cathode. Adapted with permission from Ref. [103]. Copyright (2020) Elsevier.

fore, the battery exhibited a long-term cycling stability (94% retention after 3000 cycles). Zhang et al. prepared MnO₂-based composites by coating hydrophobic graphene and amphiphilic cellulose nano-whiskers (MNG) (Figure 12g).^[103] As shown in Figure 12(h), proper hydrophobicity of graphene greatly forces hydrated Zn²⁺ desolvation, facilitating Zn²⁺ insertion into host materials, which promotes the Zn²⁺ transportation and avoid the structural collapse caused by the insertion of a large number of hydrated Zn²⁺. Combined with the excellent conductivity of graphene and cellulose nanowhiskers (Figure 12i), the MNG cathode achieves a superior rate capacity of 196 mAh g⁻¹ at an extremely high current density of 20 C and an excellent cycle stability (Figure 12j, k).

3.2.2. Conductive Polymers

Conductive polymers have the advantages of easy synthesis, low cost, and good conductivity. Currently, reports of conductive polymers compound with manganese-based materials mainly focus on the polypyrrole (PPy).^[76,108,109] Liu et al. developed a 3D PPy-encapsulated Mn₂O₃ composite, in which the PPy not only formed a conductive network for fast electron transport but also act as a coating preventing structural damage (Figure 13a, b).^[108] The crystal structure had no

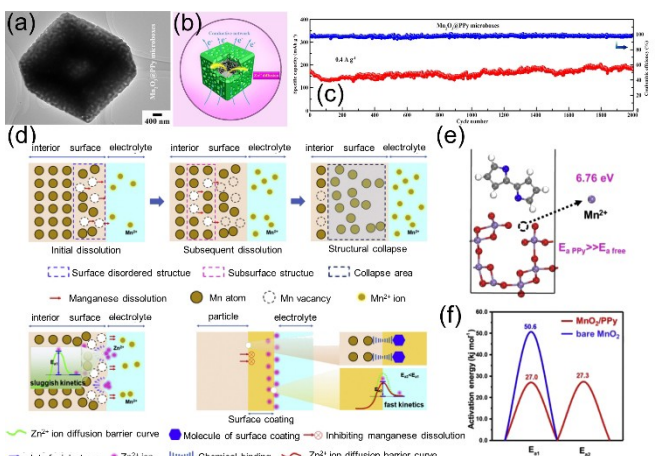


Figure 13. a) TEM of Mn₂O₃@PPy microbox, b) schematic diagram of Mn₂O₃@PPy cathode, c) ex-situ XRD patterns of Mn₂O₃@PPy. Adapted with permission from Ref. [108]. Copyright (2019) American Chemical Society. d) Schematic diagram of the problems and proposed ideal model of manganese-based cathode materials, e) energy barrier to remove Mn atom, f) activation energy of charge transfer process of bare MnO₂ and MnO₂/PPy. Adapted with permission from Ref. [110]. Copyright (2020) Elsevier.

significant variation during charge and discharge, thus the battery suggests a high-rate performance and long-term stability (no capacity decay over 2000 cycles) (Figure 13c).

Recently, Huang et al. further pointed out that PPy coating has advantages on preventing the dissolution of Mn²⁺ and improving the sluggish interfacial kinetics.^[110] As shown in Figure 13(d), structural damage of MnO₂ can be attributed to the dissolution of surface atoms and a series of chain reactions and the high diffusion barrier caused by electrostatic repulsion will slow down the sluggish interfacial kinetics. When PPy is introduced as a coating, the Mn atom on the surface will bond with the N atom in PPy to form a strongly Mn–N bonding. This greatly increases the energy barrier to remove manganese atoms (E_a free = 0.26 eV) (Figure 13e), which is effective to prevent the dissolution problems. The PPy coating reduces the energy barrier for the charge transfer process, thus achieving the fast reaction kinetics (Figure 13f).

Other conductive polymers such as polyaniline (PANI) and polyacrylic acid (PAA) have also been reported. Mao et al. used PANI as a coating for the composite aerogel of MnO₂/rGO.^[111] The PANI coating not only provides excellent conductivity, but also effectively inhibits the dissolution of Mn²⁺. Recently, Zhang et al. reported a freestanding MnO₂/CNT/PAA cathode for ZIBs,^[112] in which PAA plays a unique advantage on achieving excellent mechanical and electrical properties.

3.2.3. Others

Besides carbon materials and conductive polymers, layered MXene, owing to the typical accordion structure with large interlayer spacing, large specific surface area, excellent electrical conductivity and structural stability, is also composited with manganese-based compounds.

Zhu et al. prepared K-V₂C@MnO₂ with MnO₂ nanosheets formed on the V₂CT_x MXene surface (Figure 14a, b).^[113] Due to the lower electron affinity of V₂C (3.84 eV), the electrons tend to transfer into the conduction band of MnO₂, increasing the density of states of MnO₂ near the Fermi level, which significantly increase the electronic conductivity of K-V₂C@MnO₂ (Figure 14c, d). In addition, the lower Gibbs free energy of Zn²⁺ adsorption of K-V₂C@MnO₂ (-0.74 eV) delivers the fast ion transport kinetics and high reversibility of ion adsorption/desorption (Figure 14e), resulting in high rate

capacity of 87.7 mAh g^{-1} at 15 A g^{-1} . Luo et al. created a nanoscale parallel circuitry based on manganese decorated MXene (MnO_x@Ti₃C₂T_x).^[114] Layered MXene provided a parallel circuitry for fast ion transport, and the Ti₃C₂T_x stacks improve the electron conductivity. Thus, the MnO_x@Ti₃C₂T_x possess a high rate performance of $130 \text{ mAh g}_{(\text{Mn})}^{-1}$ at an extremely high current density $30 \text{ A g}_{(\text{Mn})}^{-1}$.

Shi et al. synthesized a 3D assembly of MXene-stabilized ZnMn₂O₄ through hydrothermal method.^[69] The ZnMn₂O₄ nanoparticles are evenly anchored on the MXene without obvious aggregation (Figure 14f). The MXene effectively inhibits the structural degradation and side reaction of ZnMn₂O₄ (Figure 14g), which is contributed to the long cycle performance of 92.4% retention after 5000 cycles at 1 A g^{-1} (Figure 14h). They also prepared 3D Ti-MXene@MnO₂ microflowers for the cathode in ZIBs.^[115] The 3D microflower structure with a robust skeleton could prevent the structural collapse during cycling and avoid the direct contact between MnO₂ nanoparticles and electrolyte, which greatly inhibits the dissolution of Mn²⁺. As a result, the cathode delivers an outstanding cycle stability over 2000 cycles. Manganese-based composite materials are shown in Table 2.

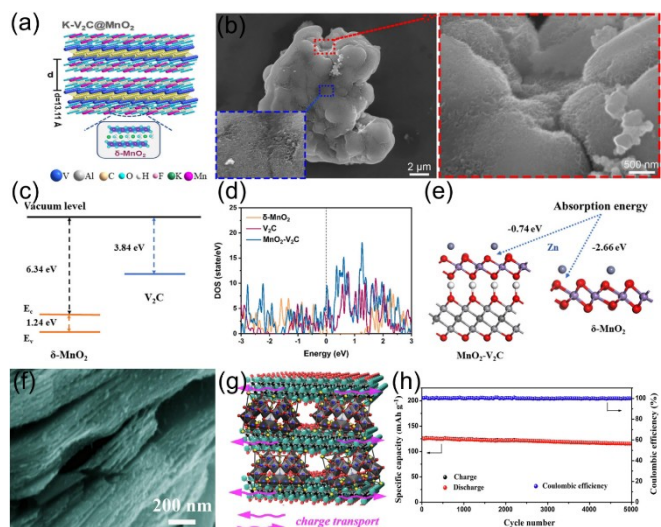


Figure 14. a) Schematic illustration of K-V₂C@MnO₂, b) SEM image of K-V₂C@MnO₂, c) band edge positions of $\delta\text{-MnO}_2$ and V₂C, d) DOS calculations of $\delta\text{-MnO}_2$, V₂C, and MnO₂-V₂C. e) Absorption energies of Zn²⁺ on the surfaces of $\delta\text{-MnO}_2$ and MnO₂-V₂C. Adapted with permission from Ref. [108]. Copyright (2021) American Chemical Society. f) SEM image of ZnMn₂O₄@Ti₃C₂T_x, g) schematic illustration of MXene-stabilized ZnMn₂O₄, h) cycle performance at 1 A g^{-1} of ZnMn₂O₄@Ti₃C₂T_x cathode. Adapted with permission from Ref. [110]. Copyright (2020) Elsevier.

3.3. Pre-Intercalation

The incorporation of conductive agents shares advantages on improving the conductivity and preventing the Mn²⁺ dissolution of manganese-based cathode materials, while suggesting little effect on the manganese-based compound itself. Pre-intercalated crystal water, ions and molecules in the manganese-based compound, will expand the interlayer spacing, reducing the diffusion resistance of ions and serve as "structural pillar", stabilizing the structure of the manganese-based compound during repeated Zn²⁺ insertion/extraction.

Table 2. Electrochemical properties of manganese-based cathode materials composited with conductive materials.							
Cathode	Anode	Electrolyte	Voltage [V]	Maximum capacity [mAh g ⁻¹]/current density [A g ⁻¹]	Rate performance: capacity [mAh g ⁻¹]/current density [A g ⁻¹]	Retention/cycles/current density [A g ⁻¹]	Ref.
ZnMn ₂ O ₄ @porous carbon	Zn plate	1 M ZnSO ₄ + 0.05 M MnSO ₄	0.8–1.8	176.8/100	88.7/4	90.3%/2000/1000	[68]
MnO _x @N-doped carbon	Zn foil	2 M ZnSO ₄ + 0.1 M MnSO ₄	0.8–1.8	385/0.1	100/2	~100%/1600/2	[99]
cellulose/graphene/MnO ₂	Zn foil	2 M ZnSO ₄ + 0.2 M MnSO ₄	0.8–1.9	384/0.3	196/9	52.68%/5000/6	[103]
Mn ₂ O ₃ @C/CNT fibers	Zn/CNT fibers	2 M ZnSO ₄ + 0.5 M MnSO ₄	1.0–1.8	253.1/0.5	147.5/5	79.6%/3000/5	[104]
MnO ₂ @N-doped hollow carbon spheres	Zn foil	3 M ZnSO ₄ + 0.15 M MnSO ₄	1.0–1.85	349/0.1	100/2	78.7%/2000/2	[105]
ZnMn ₂ O ₄ /N-doped graphene	Zn foil	1 M ZnSO ₄ + 0.05 M MnSO ₄	0.8–1.8	221/0.1	75/2	97.4%/2500/1	[106]
MnO ₂ /graphene scrolls	Zn foil	2 M ZnSO ₄ + 0.2 M MnSO ₄	0.8–1.8	362.2/0.3	145.3/3	94%/3000/3	[107]
Mn ₂ O ₃ @PPy	Zn foil	2 M ZnSO ₄ + 0.1 M MnSO ₄	1.0–1.8	255/0.1	75.6/2	~100%/2000/0.4	[108]
MnO _x /PPy	Zn foil	2 M ZnSO ₄ + 0.1 M MnSO ₄	1.0–1.8	408/0.3	67/3	78%/2800/1.5	[109]
MnO ₂ /PPy	Zn foil	2 M ZnSO ₄ + 0.1 M MnSO ₄	0.8–1.8	256/0.1	90/1.5	100%/500/1	[110]
MnO ₂ /GO/PANI	Zn foil	2 M ZnSO ₄	0.8–1.8	241.1/0.1	111.7/1	82.7%/600/1	[111]
MnO ₂ /CNT/PAA	Zn foil	2 M ZnSO ₄ + 0.1 M MnSO ₄	1.0–1.9	302/0.3	103/3	82%/1000/1.5	[112]
K-V ₂ C@MnO ₂	Zn sheet	2 M ZnSO ₄ + 0.25 M MnSO ₄	0.8–1.8	316.3/0.3	87.7/15	~100%/10000/10	[113]
MnO _x @Ti ₃ C ₂ T _x	Zn foil	2 M ZnSO ₄ + 0.2 M MnSO ₄	0.8–1.8	270/0.1	130/30	~100%/400/5	[114]
Ti ₃ C ₂ T _x @MnO ₂	Zn foil	2 M ZnSO ₄ + 0.1 M MnSO ₄	0.8–1.8	301.2/0.1	202.2/2	90.6%/2000/0.5	[115]

3.3.1. Crystal Water

Pre-intercalated crystal water in manganese-based compound can effectively expand the interlayer spacing and weaken the electrostatic interaction between Zn^{2+} and $[MnO_6]$ skeleton, which is beneficial to the Zn^{2+} diffusion. Nam et al. prepared a crystal water pre-inserted MnO_2 layered structure (cw- MnO_2), which possesses a larger interlayer spacing of 7.3 Å than that of pure MnO_2 (7.0 Å) (Figure 15a).^[116] One the one hand, the cw- MnO_2 delivers a lower energy barrier of Zn migration of 0.25 eV, much lower than the migration energy of Zn^{2+} in MnO_2 (1.03 eV) (Figure 15b), which suggests the fast Zn^{2+} diffusion. One the other hand, in cw- MnO_2 , the escaped Mn^{2+} is difficult to form the freely movable $[Mn(H_2O)_6]^{2+}$, but exists in the form of stable Zn–Mn dumbbell structure (Figure 15c), thereby effectively inhibiting the dissolution of Mn^{2+} . Therefore, the cw- MnO_2 cathode exhibits an excellent rate capacity of 150.0 mAhg⁻¹ at 3 Ag⁻¹ and long cycle stability with 75.3% retention after 200 cycles.

Jiang et al. further predicted the transport behavior of Zn^{2+} and H^+ in crystal water pre-inserted MnO_2 through the ab initio molecular dynamics (AIMD) simulation.^[117] Driven by H_2O molecules, the Zn^{2+} and H^+ could co-exist stably and transmit smoothly between the layers of MnO_2 without damaging the layered structure (Figure 15d–f), which makes an explanation for the improved rate performance and long cycle stability up to 10000 cycles (Figure 15g, h).

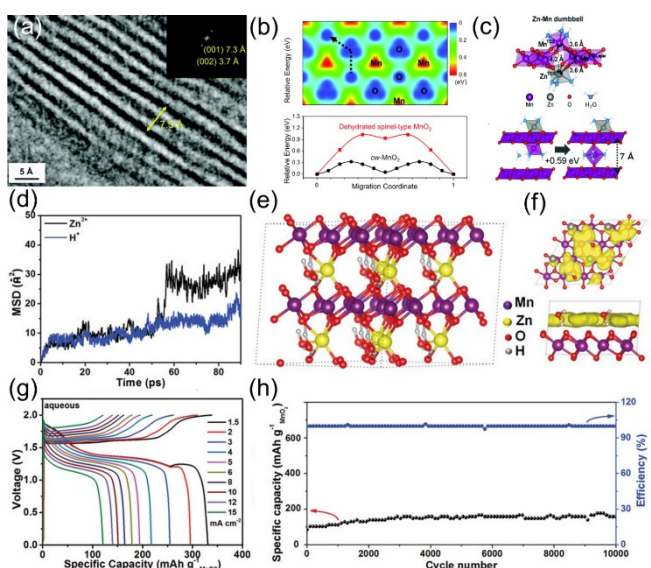


Figure 15. a) HRTEM of cw- MnO_2 , b) the migration pathway and barriers of Zn^{2+} in cw- MnO_2 , c) schematic diagram of Zn–Mn dumbbell structure and complexation behavior of Mn-octahedra. Adapted with permission from Ref. [117]. Copyright (2019) Royal Society of Chemistry. d) Mean square displacements of Zn^{2+} and H^+ in MnO_2 , e) schematic diagram of Zn^{2+} and H^+ intercalated structure, f) diffusion trajectories of Zn^{2+} and H^+ , g) GCD curves at different current densities, h) cycle performance at 5 $mA\text{cm}^{-2}$. Adapted with permission from Ref. [117]. Copyright (2020) Wiley-VCH.

3.3.2. Ions

Pre-intercalated ions in the manganese-based compound not only adjusts the interlayer spacing to accelerate ion transfer, but also plays a supporting role for improving the structural stability of the manganese-based cathode materials. Zhai et al. prepared layered $Na_{0.55}Mn_2O_4 \cdot 0.57H_2O$ with Na^+/H_2O co-intercalated MnO_2 .^[118] As shown in Figure 16a, b, during the first cycle, Na^+ acts as the pillar for Zn^{2+} insertion upon discharge progress. And then, the Zn^{2+} replaces part of Na^+ to stabilize the interlayers during the following discharge/charge process. Therefore, the cathode shows an excellent rate and cycle performance with a high capacity of 201.6 mAhg⁻¹ at 0.5 Ag⁻¹ after 400 cycles.

Guo et al. prepared a Ca_2MnO_4 (CMO) cathode with Ca^{2+} pre-intercalated into MnO_2 .^[119] In the first charging process, the pre-intercalated Ca^{2+} releases from the CMO and forms a single-component $CaSO_4 \cdot 2H_2O$ (CS) solid electrolyte interface (SEI) film on the surface of CMO (Figure 16c). Ca^{2+} pre-intercalation could improve ion/electron kinetics and stable structure of MnO_2 , and the CS SEI film further reduces the interface activation energy (Figure 16d), promoting the insertion/extraction of Zn^{2+} and inhibits the dissolution of Mn^{2+} ,

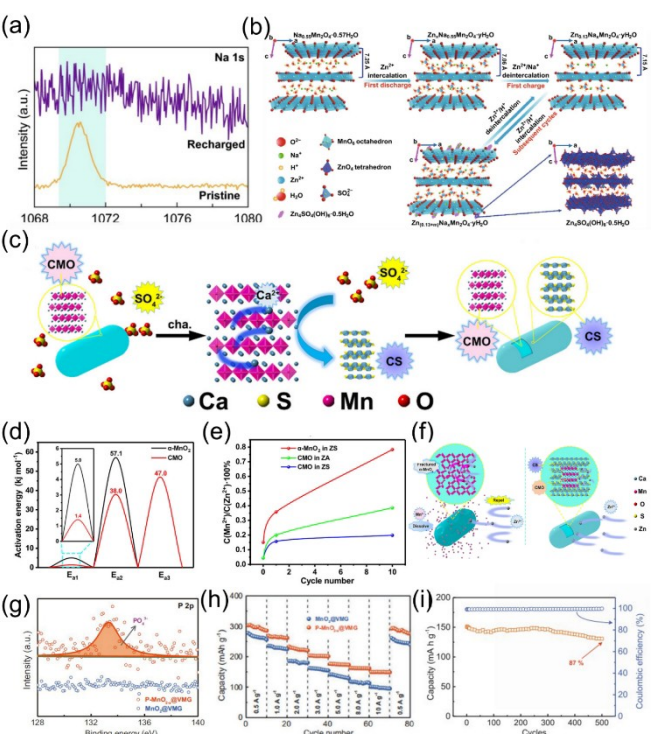


Figure 16. a) XPS Na 1s spectra at different statuses of $Na_{0.55}Mn_2O_4 \cdot 0.57H_2O$, b) schematic illustration in discharge/charge processes of $Na_{0.55}Mn_2O_4 \cdot 0.57H_2O$ cathode. Adapted with permission from Ref. [118]. Copyright (2020) Springer. c) Formation mechanism of CS SEI film, d) activation energy curve of MnO_2 and CMO, e) manganese dissolution rate of MnO_2 and CMO, f) schematic diagram of reaction mechanism of MnO_2 and CMO cathode. Adapted with permission from Ref. [119]. Copyright (2019) American Chemical Society. g) XPS P 2p spectra of MnO_2 @VMG and P- MnO_{2-x} @VMG, h) rate performance and (i) cycle performance at 5 Ag^{-1} of P- MnO_{2-x} @VMG cathode. Adapted with permission from Ref. [121]. Copyright (2020) Wiley-VCH.

improving the structural stability of CMO (Figure 16e, f). As a result, the CMO cathode achieves a specific capacity of 100 mAh g^{-1} at 1 A g^{-1} and there is no obvious capacity fading after 1000 cycles. Similarly, Sun et al. prepared Ca^{2+} and H_2O as pillars pre-inserted layered $\delta\text{-MnO}_2$ ^[120] noted as $\text{Ca}_{0.28}\text{MnO}_2 \cdot 0.5\text{H}_2\text{O}$, which possess a capacity of 100.9 mAh g^{-1} at 3.5 A g^{-1} even after 5000 cycles.

Apart from cations, anion (PO_4^{3-}) was also pre-intercalated into MnO_2 (Figure 16g).^[121] The pre-intercalated PO_4^{3-} expands the interlayer spacing from 0.68 to 0.70 nm, accelerating the Zn^{2+} diffusion. Under the synergistic effect of vertical multilayer graphene arrays and oxygen defects, the cathode delivers an impressive high-rate capacity (150.1 mAh g^{-1} at 10 A g^{-1}), and excellent cycle performance (91.3% retention after 1000 cycles) (Figure 16h, i).

3.3.3. Molecules

Apart from cations/anions, polymer molecules, such as PANI, PPy, etc., are also adopted to pre-intercalated into the MnO_2 for an excellent electrochemical performance. Huang et al. prepared polyaniline (PANI)-intercalated MnO_2 through an inorganic/organic interface reaction (Figure 17a).^[122] The intercalated PANI molecules not only enlarge the interlayer space of MnO_2 (Figure 17b), improving ion diffusion kinetics, but also strengthen the layered structure, avoiding the phase change and structural collapse during ion insertion/extraction. Based on the co-insertion/ extraction mechanism of H^+ and Zn^{2+} , the battery achieved a high capacity of 110 mAh g^{-1} at 3 A g^{-1} and a cycle stability of 200 cycles (Figure 17c, d).

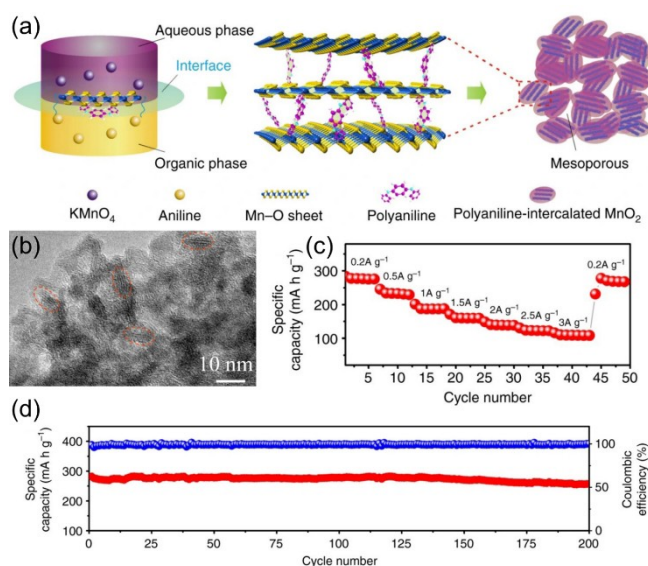


Figure 17. a) Schematic illustration of PANI-intercalated MnO_2 , b) HTEM of PANI-intercalated MnO_2 , c) rate performance and d) cycle performance at 0.2 A g^{-1} of PANI-intercalated MnO_2 cathode. Adapted with permission from Ref. [122]. Copyright (2018) Springer Nature.

3.4. Defect Engineering

Fragile crystal structure and strong ion insertion barrier by electrostatic repulsion between Zn^{2+} and manganese-based compounds severely limit the electrochemical performance. Defect engineering is expected to modify the crystal structure, and then reduce the ion insertion barrier.^[123–125] The defect engineering strategies for manganese-based cathode materials mainly focus on oxygen vacancy, cation vacancy and cationic doping.

3.4.1. Oxygen Vacancy

Oxygen vacancy can not only change the thermodynamics of the electrode surface, increase the active sites, but also adjust the electronic structure to promote the transfer of electrons and ions. Xiong et al. prepared oxygen-deficient MnO_2 as the cathode material for ZIBs (Figure 18a).^[126] As shown in Figure 18(b, c), due to the oxygen vacancy, the Gibbs free energies of Zn^{2+} adsorption near the vacancies are close to thermoneutral values (0.05 eV), which indicates that the adsorbed Zn^{2+} are easier to desorb, and then the once-occupied active surface areas could be accessible for the next Zn^{2+} adsorption. The high reversibility of Zn^{2+} adsorption/desorption results that oxygen-deficient MnO_2 cathode displays a high specific

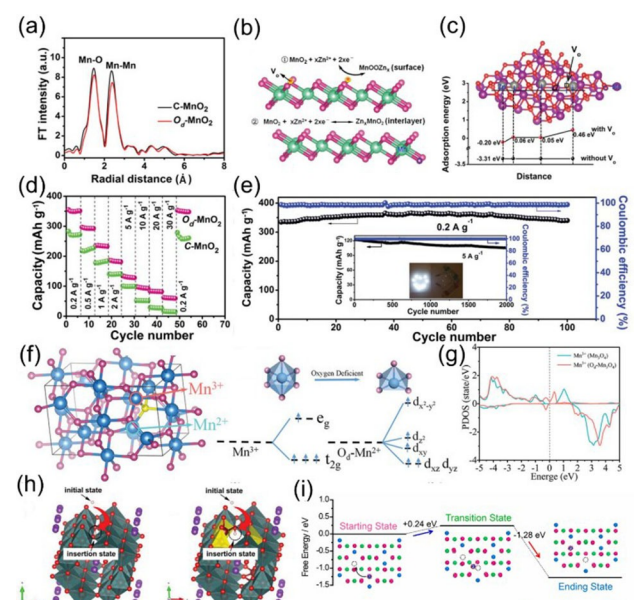


Figure 18. a) k^3 -weighted Fourier transform of the extended X-ray absorption fine structure data of $\text{O}_d\text{-MnO}_2$ and C-MnO₂, b) mechanisms of $\text{D}_d\text{-MnO}_2$ for Zn^{2+} storage, c) Zn^{2+} adsorption energies of $\text{O}_d\text{-MnO}_2$ and C-MnO₂, d) rate performance and e) cycle performance at 0.2 A g^{-1} and 5 A g^{-1} of $\text{O}_d\text{-MnO}_2$ cathode. Adapted with permission from Ref. [126]. Copyright (2019) Wiley-VCH. f) octahedral and pyramidal crystal fields and the d-orbital splitting configurations of $\text{O}_d\text{-Mn}_2\text{O}_4$, g) partial DOS of Mn^{3+} atom around the oxygen vacancy. Adapted with permission from Ref. [127]. Copyright (2020) Wiley-VCH. h) H^+ storage path in ab-plane of perfect and oxygen-defect MnO_2 . Adapted with permission from Ref. [128]. Copyright (2019) Wiley-VCH. i) energy profiles of the Zn diffusion in $\text{O}_d\text{-ZnMn}_2\text{O}_4$. Adapted with permission from Ref. [129]. Copyright (2019) Elsevier.

capacity of 345 mAh g^{-1} at 0.2 A g^{-1} , a superior rate capacity at 30 A g^{-1} and a capacity retention of 84% after 2000 cycles at 5 A g^{-1} (Figure 18d, e).

Tan et al. explored the effect of oxygen vacancy on the electrical conductivity of Mn_3O_4 .^[127] After introducing oxygen vacancy, the octahedral crystal of Mn^{3+} changes to form a pyramidal crystal field, increasing the Mn^{3+} charge density (Figure 18f) and the bandgap changes to 0 eV (Figure 18g), thereby improving the conductivity. Fang et al. confirmed that oxygen vacancies are essential for the fast H^+ diffusion through opening the $[\text{MnO}_6]$ polyhedral wall and creating additional ion channels in the deformed $[\text{MnO}_6]$ polyhedral (Figure 18h).^[128] Zhang et al. also simulated the diffusion kinetics of Zn^{2+} in the ZnMn_2O_4 .^[129] The energy barrier of Zn^{2+} mobility near oxygen vacancy is 0.24 eV, much lower than that in perfect ZnMn_2O_4 (0.39 eV) (Figure 18i), which indicates the rapid Zn^{2+} diffusion in oxygen-deficient ZnMn_2O_4 . These all confirm that oxygen vacancy plays a vital role in promoting ion/electron transfer and stabilizing the crystal structure, leading to an excellent electrochemical performance of manganese-based cathode materials.

3.4.2. Cation Vacancy

Cation vacancy could weak the electrostatic interaction between the ions and the host lattice and then promote the insertion of ions into the host, which have been applied in various ion batteries.^[130–133] In the field of ZIBs, Mn vacancy is the most common cation vacancies in manganese-based cathode materials. Zhu et al. prepared a $\text{Mn}_{0.61}\square_{0.39}\text{O}$ (\square refers to Mn defect) cathode with Mn defects (Figure 19a) and analyzed the influence of Mn vacancy through DFT calculations.^[134] On the one hand, Mn vacancy increases the charge density around the Fermi level (Figure 19b), improving the conductivity of MnO . On the other hand, Mn vacancy creates the large channels for Zn^{2+} insertion and available active sites for Zn^{2+} storage, effectively avoiding the structural collapse during the repeated insertion/extraction (Figure 19c). With the carbon coating, the $\text{Mn}_{0.61}\square_{0.39}\text{O}$ cathode possess a high capacity of 116 mAh g^{-1} at 1 A g^{-1} after 1500 cycles (Figure 19d).

In addition, Zhang et al. clarified the kinetics and mechanism of Zn^{2+} insertion/extraction in ZnMn_2O_4 with Mn vacancy.^[135] As shown in Figure 19(e, f), in perfect ZnMn_2O_4 , the large electrostatic repulsion of Mn cations at octahedral sites strongly hindered the Zn^{2+} diffusion between adjacent tetrahedrons. While the Mn vacancy weakens this electrostatic barrier, resulting in the fast Zn^{2+} diffusion kinetics. Thus, the cation-defected ZnMn_2O_4 exhibits a remarkable electrochemical performance.

3.4.3. Cation Doping

Cation doping into the manganese-based compounds to change the lattice spacing of the crystal structure, is also a

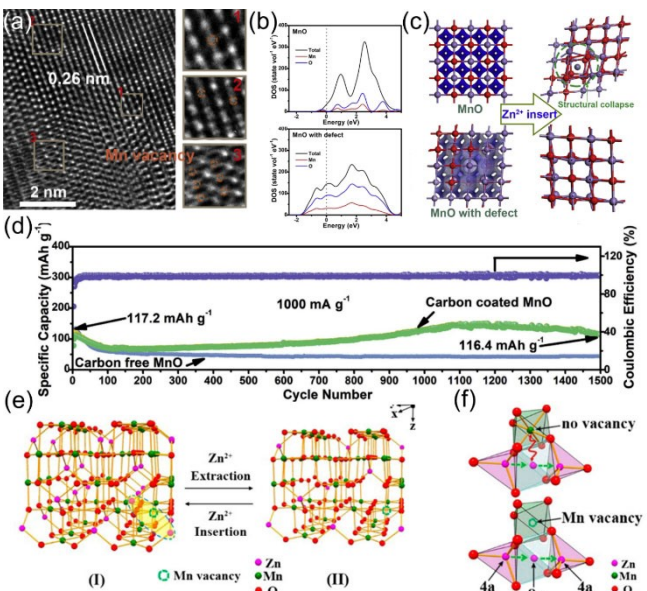


Figure 19. a) HRTEM image of $\text{Mn}_{0.61}\square_{0.39}\text{O}$, b) calculated density of states of MnO and $\text{Mn}_{0.61}\square_{0.39}\text{O}$, c) charge distribution and structures after Zn^{2+} insertion of MnO and $\text{Mn}_{0.61}\square_{0.39}\text{O}$, d) cycle performance at 1 A g^{-1} . Adapted with permission from Ref. [134]. Copyright (2020) Elsevier. e) Schematic illustration of Zn^{2+} insertion/extraction in ZnMn_2O_4 with Mn vacancy, f) Zn^{2+} diffusion pathway in ZnMn_2O_4 without and with Mn vacancy. Adapted with permission from Ref. [135]. Copyright (2016) American Chemical Society.

feasible strategy to improve the energy storage performance. Zhang et al. prepared Ni-doped Mn_3O_4 (NM20) with the atomic ratio of Ni and Mn in the precursor 1:20 (Figure 20a).^[136] Ni doping increases the charge density around the Fermi level (Figure 20b), thereby increasing the electronic conductivity of NM20. In addition, in NM20, the extra electrons are accumulated around the Mn atoms adjacent to the doped Ni atoms (Figure 20c), generating the strong interaction between the Mn and O atoms, which greatly enhances the structural stability. As a result, NM20 cathode exhibits a discharge capacity of 132 mAh g^{-1} at 1 A g^{-1} and a superior cycle stability of 85.6% retention over 2500 cycles (Figure 20d, e).

Ji et al. prepared a multi-valence cobalt-doped Mn_3O_4 ,^[137] in which the Co^{2+} doping acts as “structural pillar”, effectively improving the structural stability, the $\text{Co}^{2+/3+}$ doping inhibits the Jahn-Teller effect and promotes ion diffusion, and the Co^{4+} increases the conductivity (Figure 20f).

Tao et al. reported a Ni and Co co-substituted ZnMn_2O_4 as the cathode for ZIBs.^[138] The Co and Ni replaced Mn in the octahedral sites (Figure 20g), which increases the lattice parameters and then promotes the Zn^{2+} diffusion. Moreover, the co-doping of Ni and Co also inhibits the Jahn-Teller distortion of Mn^{3+} and stabilizes the crystal structure. Benefit from this, the Ni and Co co-doped ZnMn_2O_4 cathode shows a stable capacity of 117.7 mAh g^{-1} after 600 cycles at 0.5 A g^{-1} .

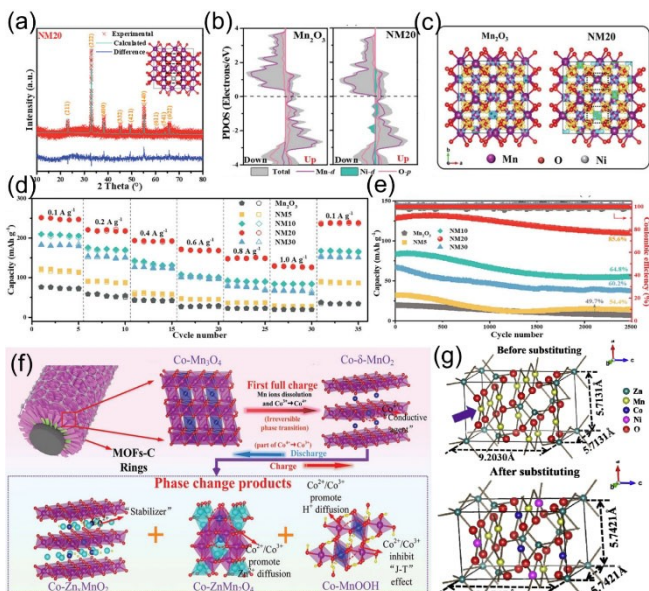


Figure 20. a) Rietveld refinement results of NM20, b) density of states of Mn_2O_3 and NM20, c) electron density of Mn_2O_3 and NM20, d) rate performance and e) cycle performance at 1.0 A g^{-1} of NM cathode. Adapted with permission from Ref. [136]. Copyright (2021) Wiley-VCH. f) Schematic illustration of the multi-valence cobalt-doped Mn_3O_4 . Adapted with permission from Ref. [137]. Copyright (2021) Wiley-VCH. g) Crystal structure of ZnMn_2O_4 with and without Ni and Co co-doping. Adapted with permission from Ref. [138]. Copyright (2020) Elsevier.

3.5. Electrochemical Activation

The ZnSO_4 or $\text{Zn}(\text{CF}_3\text{SO}_3)_2$ aqueous solution is used as the electrolytes of ZIBs. Due to the weakly acidic, manganese-based cathode materials will slowly dissolve into electrolytes.^[34] Adding Mn^{2+} to the electrolyte in advance not only changes the dissolution equilibrium of Mn^{2+} , inhibiting its dissolution, but also the Mn^{2+} in the electrolyte contributes to the capacity of the cathode materials.^[139] This is mainly due to the fact that Mn^{2+} can be electro-oxidized into active MnO_2 .^[27,140] Inspired by this, manganese-based cathode materials without electrochemically active are expected to be activated via in situ electrochemical charging. Notably, the activation process is often accompanied by phase change and occurs in the initial cycles.

Hao et al. proposed electrochemically induced spinel-layered phase transition of Mn_3O_4 .^[67] As displayed in Figure 21(a, b), when charging up to 1.9 V, with the dissolution of Mn^{2+} and oxidation of Mn^{3+} to Mn^{4+} , Mn_3O_4 was oxidized to Mn_5O_8 intermediate and further transformed into layered Zn -birnessite for Zn^{2+} insertion/extraction. As a result, the capacity of Mn_3O_4 cathode gradually increases from 85.6 to 239.2 mAh g^{-1} at 0.1 A g^{-1} (Figure 21c), and a superior rate and cycle performance is achieved (Figure 21d, e).

In principle, MnO with divalent manganese is electrochemically inactive, but it can also store Zn^{2+} after electrochemical activation. Li et al. analyzed the activation process of MnO through ex-situ XPS and XRD tests (Figure 21f-h).^[141] With the dissolution of Mn^{2+} , the valence of Mn continues to rise in the

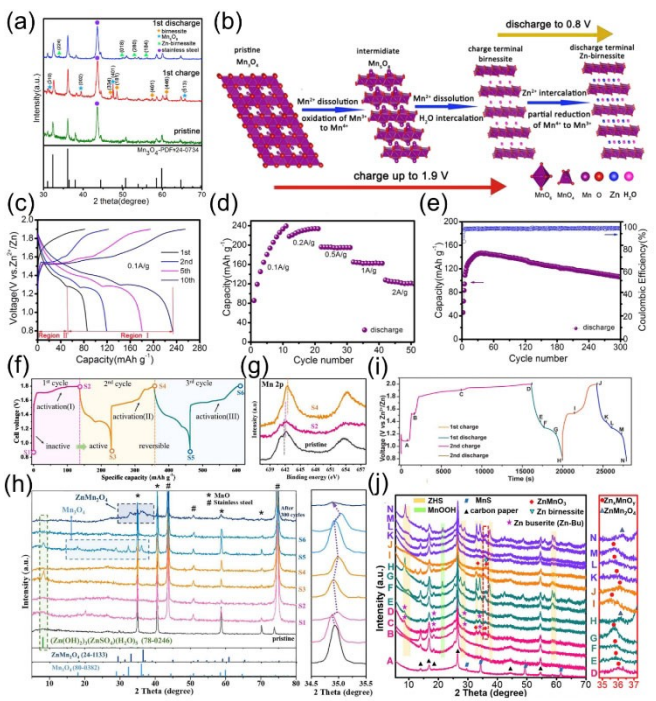


Figure 21. a) Ex-situ XRD of Mn_3O_4 at first cycle, b) reaction pathway of Mn_3O_4 in the first cycle, c) GCD curves of different cycles at 0.1 A g^{-1} , d) rate performance and e) cycling performance at 0.5 A g^{-1} of Mn_3O_4 cathode. Adapted with permission from Ref. [67]. Copyright (2018) Elsevier. f) discharge/charge profiles for the first 3 cycles of MnO cathode, g) ex-situ XPS and h) XRD of MnO . Adapted with permission from Ref. [141]. Copyright (2020) Elsevier. i) GCD curve of the first two cycles of MnS -EDO cathode, j) ex-situ XRD of MnS -EDO. Adapted with permission from Ref. [143]. Copyright (2020) Elsevier.

first 2 cycles, and the MnO changes to Mn_3O_4 for Zn^{2+} and H^+ insertion/extraction. Similarly, commercial MnO particles were oxidized to porous layered-type MnO_2 nanosheets through the electrochemical activation,^[142] which indicates that the originally inactive MnO could act as the cathode material of ZIBs directly, and exhibit an excellent electrochemical performance.

In addition, Chen et al. reported an electrochemically derived oxide (MnS -EDO) from MnS through in situ electrochemical activation (Figure 21i, j).^[143] In the first charge, inactive MnS is completely transformed to Zn buserite and ZnMnO_3 for Zn^{2+} and H^+ insertion/extraction. The MnS -EDO demonstrates a large number of active sites, high electrochemical reactivity, fast ion diffusion kinetics, and excellent structural stability, thus exhibiting an outstanding rate capability and long-term stability with a capacity of 104 mAh g^{-1} after 4000 cycles at 3 A g^{-1} .

4. Conclusion and Perspectives

Among the various cathode materials, manganese-based cathode materials with the unique advantages such as low cost, non-toxic, high specific capacity (308 mAh g^{-1}) and operating voltage ($\sim 1.4 \text{ V}$), are very competitive for ZIBs compared with others.

Herein, first, various synthetic methods of manganese-based cathode materials are summarized, including hydrothermal method, electrodeposition method, redox reaction method, etc. Different methods affect the morphology and structure of manganese-based cathode materials and then affect the specific capacity, rate performance and cycle stability.

The inherent poor conductivity, Mn^{2+} dissolution and structural instability of manganese-based cathode materials make it difficult to reach the theoretical specific capacity. What's more, the rate performance and cycle performance are also unsatisfactory, which severely restricts its application. 5 performance optimization strategies are analyzed in detail, as follows:

- (1) Structure design: Nanostructures improve the specific surface area and ion diffusion, providing more active sites for energy storage and promoting the fast ion/electron kinetics, and the porous and hollow structures significantly alleviate the volume change, improving the structural stability.
- (2) Compositing with conductive materials: The composite materials not only retain the high capacity of manganese itself, but also exert the excellent conductivity of another component.
- (3) Pre-intercalation: It is able to expand the layer spacing, thereby promoting the ion insertion/extraction. Furthermore, the pre-intercalated crystal water, ions, and molecules act as "structural pillars" to avoid the structural collapse.
- (4) Defect engineering: Defect engineering modifies the crystal structure, thus substantially improving the conductivity and structural stability and the introduction of defects provides more ion intercalation channels and active sites, which is beneficial to the fast electrochemical kinetic process.
- (5) Electrochemical activation: The charging and discharging process itself is an electrochemical activation process. Especially, this strategy can activate the manganese-based compounds without electrochemical activity, such as MnO .

At present, the above 5 strategies have been applied to optimize the performance of manganese-based cathode materials. Apart from them, the following strategies may be feasible to improve the performance:

- (1) Design of the heterostructure: The properties of heterostructure arise from the contributions of each component as well as from processes that occur at the interfaces between the components. Therefore, well-designed heterostructures may help improve the performance of manganese-based cathode materials.
- (2) Modification of surface or interface: It is noteworthy that with the charge transfer and ion diffusion, the structure of surface or interface will change, which has a great impact on the electrochemical properties. At present, coating can be regarded as a surface modification method. Other methods and modification mechanisms are worthy of consideration.

Conflict of Interest

The authors declare no conflict of interest.

Keywords: manganese-based cathode materials · performance optimization · synthesis · zinc-ion batteries

- [1] Z. Yang, J. Zhang, M. C. W. Kintner-Meyer, X. Lu, D. Choi, J. P. Lemmon, J. Liu, *Chem. Rev.* **2011**, *111*, 3577.
- [2] S. Chu, A. Majumdar, *Nature* **2012**, *488*, 294.
- [3] S. Chu, Y. Cui, N. Liu, *Nat. Mater.* **2017**, *16*, 16.
- [4] B. Dunn, H. Kamath, J.-M. Tarascon, *Science* **2011**, *334*, 928.
- [5] X. Wang, X. Lu, B. Liu, D. Chen, Y. Tong, G. Shen, *Adv. Mater.* **2014**, *26*, 4763.
- [6] D. Larcher, J. M. Tarascon, *Nat. Chem.* **2015**, *7*, 19.
- [7] G. Zubi, R. Dufo-Lopez, M. Carvalho, G. Pasaoglu, *Renewable Sustainable Energy Rev.* **2018**, *89*, 292.
- [8] M. Li, J. Lu, Z. Chen, K. Amine, *Adv. Mater.* **2018**, *30*, 1800561.
- [9] G. Assat, J.-M. Tarascon, *Nat. Energy* **2018**, *3*, 373.
- [10] W. Lee, S. Muhammad, C. Sergey, H. Lee, J. Yoon, Y.-M. Kang, W.-S. Yoon, *Angew. Chem. Int. Ed.* **2020**, *59*, 2578.
- [11] T. Sun, Z.-J. Li, H.-G. Wang, D. Bao, F.-L. Meng, X.-B. Zhang, *Angew. Chem. Int. Ed.* **2016**, *55*, 10662.
- [12] L. Fan, X. Li, X. Song, N. Hu, D. Xiong, A. Koo, X. Sun, *ACS Appl. Mater. Interfaces* **2018**, *10*, 2637.
- [13] J. Liu, Y. Zhang, L. Zhang, F. Xie, A. Vasileff, S.-Z. Qiao, *Adv. Mater.* **2019**, *31*, 1901261.
- [14] T. Jin, Q. Han, L. Jiao, *Adv. Mater.* **2020**, *32*, 1806304.
- [15] J.-Y. Hwang, S.-T. Myung, Y.-K. Sun, *Adv. Funct. Mater.* **2018**, *28*, 1802938.
- [16] X. Wu, Y. Chen, Z. Xing, C. W. K. Lam, S.-S. Pang, W. Zhang, Z. Ju, *Adv. Energy Mater.* **2019**, *9*, 1900343.
- [17] J. Ding, H. Zhang, H. Zhou, J. Feng, X. Zheng, C. Zhong, E. Paek, W. Hu, D. Mitlin, *Adv. Mater.* **2019**, *31*, 1900429.
- [18] S. Chong, L. Sun, C. Shu, S. Guo, Y. Liu, W. Wang, H. K. Liu, *Nano Energy* **2019**, *63*, 103868.
- [19] X.-Y. Yang, J.-J. Xu, Z.-W. Chang, D. Bao, Y.-B. Yin, T. Liu, J.-M. Yan, D.-P. Liu, Y. Zhang, X.-B. Zhang, *Adv. Energy Mater.* **2018**, *8*, 1702242.
- [20] Q. Xiong, G. Huang, X.-B. Zhang, *Angew. Chem. Int. Ed.* **2020**, *59*, 19311–19319.
- [21] T. Liu, Y. Yu, X.-Y. Yang, J. Wang, X.-B. Zhang, *Small Structures* **2020**, *1*, 2000015.
- [22] K. Chen, G. Huang, X.-B. Zhang, *Chin. J. Chem.* **2021**, *39*, 32–42.
- [23] H. Li, L. Ma, C. Han, Z. Wang, Z. Liu, Z. Tang, C. Zhi, *Nano Energy* **2019**, *62*, 550.
- [24] N. Zhang, X. Chen, M. Yu, Z. Niu, F. Cheng, J. Chen, *Chem. Soc. Rev.* **2020**, *49*, 4203.
- [25] L. E. Blanc, D. Kundu, L. F. Nazar, *Joule* **2020**, *4*, 771–799.
- [26] K. Chen, D.-Y. Yang, G. Huang, X.-B. Zhang, *Acc. Chem. Res.* **2021**, *54*, 632–641.
- [27] Z. Yi, G. Chen, F. Hou, L. Wang, J. Liang, *Adv. Energy Mater.* **2021**, *11*, 2003065.
- [28] D. Selvakumaran, A. Pan, S. Liang, G. Cao, *J. Mater. Chem. A* **2019**, *7*, 18209.
- [29] S. Huang, J. Zhu, J. Tian, Z. Niu, *Chem. Eur. J.* **2019**, *25*, 14480.
- [30] C. Li, X. Zhang, W. He, G. Xu, R. Sun, *J. Power Sources* **2020**, *449*, 227596.
- [31] Y. Shi, Y. Chen, L. Shi, K. Wang, B. Wang, L. Li, Y. Ma, Y. Li, Z. Sun, W. Ali, S. Ding, *Small* **2020**, *16*, 2000730.
- [32] J. Ming, J. Guo, C. Xia, W. Wang, H. N. Alshareef, *Mat. Sci. Eng.* **2019**, *135*, 58.
- [33] X. Liu, J. Yi, K. Wu, Y. Jiang, Y. Liu, B. Zhao, W. Li, J. Zhang, *Nanotechnology* **2019**, *31*, 122001.
- [34] Y.-L Zhao, Y.-H Zhu, X.-B Zhang, *InfoMat* **2020**, *2*, 237.
- [35] V. Mathew, B. Sambandam, S. Kim, S. Kim, S. Park, S. Lee, M. H. Alfaruqi, V. Soundharajan, S. Islam, D. Y. Putro, J. Y. Hwang, Y. K. Sun, J. Kim, *ACS Energy Lett.* **2020**, *5*, 2376.
- [36] Y. Yang, Y. Tang, S. Liang, Z. Wu, G. Fang, X. Cao, C. Wang, T. Lin, A. Pan, J. Zhou, *Nano Energy* **2019**, *61*, 617.
- [37] F. Liu, Z. Chen, G. Fang, Z. Wang, Y. Cai, B. Tang, J. Zhou, S. Liang, *Nano-Micro Lett.* **2019**, *11*, 25.

- [38] C. Liu, Z. Neale, J. Zheng, X. Jia, J. Huang, M. Yan, M. Tian, M. Wang, J. Yang, G. Cao, *Energy Environ. Sci.* **2019**, *12*, 2273.
- [39] S. Liu, H. Zhu, B. Zhang, G. Li, H. Zhu, Y. Ren, H. Geng, Y. Yang, Q. Liu, C. Li, *Adv. Mater.* **2020**, *2001113*.
- [40] Z. Cao, L. Wang, H. Zhang, X. Zhang, J. Liao, J. Dong, J. Shi, P. Zhuang, Y. Cao, M. Ye, J. Shen, P. M. Ajayan, *Adv. Funct. Mater.* **2020**, *2000472*.
- [41] Y. Zhao, Y. Wang, Z. Zhao, J. Zhao, T. Xin, N. Wang, J. Liu, *Energy Storage Mater.* **2020**, *28*, 64.
- [42] H. Yao, Q. Li, M. Zhang, Z. Tao, Y. Yang, *Chem. Eng. J.* **2020**, *392*, 123653.
- [43] G. Kasiri, J. Glenneberg, A. B. Hashemi, R. Kun, F. La Mantia, *Energy Storage Mater.* **2019**, *19*, 360.
- [44] T. Xin, Y. Wang, N. Wang, Y. Zhao, H. Li, Z. Zhang, J. Liu, *J. Mater. Chem. A* **2019**, *7*, 23076.
- [45] C. Han, H. Li, R. Shi, T. Zhang, J. Tong, J. Li, B. Li, *J. Mater. Chem. A* **2019**, *7*, 23378.
- [46] R. Cang, K. Ye, K. Zhu, J. Yan, J. Yin, K. Cheng, G. Wang, D. Cao, *J. Energy Chem.* **2020**, *45*, 52.
- [47] L. Ma, S. Chen, C. Long, X. Li, Y. Zhao, Z. Liu, Z. Huang, B. Dong, J. A. Zapien, C. Zhi, *Adv. Energy Mater.* **2019**, *9*, 1902446.
- [48] P. Yu, Y. Zeng, H. Zhang, M. Yu, Y. Tong, X. Lu, *Small* **2019**, *15*, 1804760.
- [49] B. Tang, L. Shan, S. Liang, J. Zhou, *Energy Environ. Sci.* **2019**, *12*, 3288.
- [50] M. H. Alfaruqi, J. Gim, S. Kim, J. Song, J. Jo, S. Kim, V. Mathew, J. Kim, *J. Power Sources* **2015**, *288*, 320.
- [51] Q.-H. Zhao, A.-Y. Song, W.-G. Zhao, R.-Z. Qin, S.-X. Ding, X. Chen, Y.-L. Song, L.-Y. Yang, H. Lin, S.-N. Li, F. Pan, *Angew. Chem. Int. Ed.* **2021**, *60*, 4169.
- [52] N. Zhang, F. Cheng, J. Liu, L. Wang, X. Long, X. Liu, F. Li, J. Chen, *Nat. Commun.* **2017**, *8*, 405.
- [53] X. Liao, C. Pan, Y. Pan, C. Yin, *J. Alloys Compd.* **2021**, *888*, 161619.
- [54] C. Guo, H. Liu, J. Li, Z. Hou, J. Liang, J. Zhou, Y. Zhu, Y. Qian, *Electrochim. Acta* **2019**, *304*, 370.
- [55] S. Wang, W. Ma, Z. Sang, F. Hou, W. Si, J. Guo, J. Liang, D.-A. Yang, *J. Energy Chem.* **2022**, *67*, 82.
- [56] N. Liu, K. Mohanapriya, J. Pan, Y. Hu, Y. Sun, X. Liu, *J. Electrochem. Soc.* **2020**, *167*, 040517.
- [57] B. Yang, X. Cao, S. Wang, N. Wang, C. Sun, *Electrochim. Acta* **2021**, *385*, 138447.
- [58] S. Islam, M. H. Alfaruqi, J. Song, S. Kim, P. Duong Tung, J. Jo, S. Kim, V. Mathew, J. P. Baboo, Z. Xiu, J. Kim, *J. Energy Chem.* **2017**, *26*, 815.
- [59] J. Wang, J.-G. Wang, X. Qin, Y. Wang, Z. You, H. Liu, M. Shao, *ACS Appl. Mater. Interfaces* **2020**, *12*, 34949.
- [60] C. Wang, Y. Zeng, X. Xiao, S. Wu, G. Zhong, K. Xu, Z. Wei, W. Su, X. Lu, *J. Energy Chem.* **2020**, *43*, 182.
- [61] Y. Liu, X. Chi, Q. Han, Y. Du, J. Huang, Y. Liu, J. Yang, *J. Power Sources* **2019**, *443*, 227244.
- [62] Y. Zhang, S. Deng, Y. Li, B. Liu, G. Pan, Q. Liu, X. Wang, X. Xia, J. Tu, *Energy Storage Mater.* **2020**, *29*, 52.
- [63] Y. Wu, Y. Tao, X. Zhang, K. Zhang, S. Chen, Y. Liu, Y. Ding, M. Cai, X. Liu, S. Dai, *Sci. China Mater.* **2020**, *63*, 1196.
- [64] J. Wang, J.-G. Wang, H. Liu, C. Wei, F. Kang, *J. Mater. Chem. A* **2019**, *7*, 13727.
- [65] F. Tang, J. Gao, Q. Ruan, X. Wu, X. Wu, T. Zhang, Z. Liu, Y. Xiang, Z. He, X. Wu, *Electrochim. Acta* **2020**, *353*, 136570.
- [66] C. Zhu, G. Fang, J. Zhou, J. Guo, Z. Wang, C. Wang, J. Li, Y. Tang, S. Liang, *J. Mater. Chem. A* **2018**, *6*, 9677.
- [67] J. Hao, J. Mou, J. Zhang, L. Dong, W. Liu, C. Xu, F. Kang, *Electrochim. Acta* **2018**, *259*, 170.
- [68] C. Yang, M. Han, H. Yan, F. Li, M. Shi, L. Zhao, *J. Power Sources* **2020**, *452*, 227826.
- [69] M. Shi, B. Wang, Y. Shen, J. Jiang, W. Zhu, Y. Su, M. Narayanasamy, S. Angaiah, C. Yan, Q. Peng, *Chem. Eng. J.* **2020**, *399*, 125627.
- [70] Y. Lee, J. Lee, G. An, *Chem. Eng. J.* **2021**, *414*, 128916.
- [71] X. Zang, L. Li, J. Meng, L. Liu, Y. Pan, Q. Shao, C. Ning, *J. Mater. Sci. Technol.* **2021**, *74*, 52.
- [72] K. Lu, B. Song, Y. Zhang, H. Ma, J. Zhang, *J. Mater. Chem. A* **2017**, *5*, 23628.
- [73] J. Xu, Q. Gao, Y. Xia, X. Lin, W. Liu, M. Ren, F. Kong, S. Wang, C. Lin, *J. Colloid Interface Sci.* **2021**, *598*, 419.
- [74] M. H. Alfaruqi, S. Islam, V. Mathew, J. Song, S. Kim, T. Duong Pham, J. Jo, S. Kim, J. P. Baboo, Z. Xiu, J. Kim, *Appl. Surf. Sci.* **2017**, *404*, 435.
- [75] B. Ding, P. Zheng, P. A. Ma, J. Lin, *Adv. Mater.* **2020**, *32*, 1905823.
- [76] Z. Li, Y. Huang, J. Zhang, S. Jin, S. Zhang, H. Zhou, *Nanoscale* **2020**, *12*, 4150.
- [77] X. Jia, C. Liu, Z. G. Neale, J. Yang, G. Cao, *Chem. Rev.* **2020**, *120*, 7795.
- [78] W. Sun, F. Wang, S. Hou, C. Yang, X. Fan, Z. Ma, T. Gao, F. Han, R. Hu, M. Zhu, C. Wang, *J. Am. Chem. Soc.* **2017**, *139*, 9775.
- [79] F. Kataoka, T. Ishida, K. Nagita, V. Kumbhar, K. Yamabuki, M. Nakayama, *ACS Appl. Energ. Mater.* **2020**, *3*, 4720.
- [80] A. Dhiman, D. G. Ivey, *Batteries & Supercaps* **2020**, *3*, 293.
- [81] K. Wang, X. Zhang, J. Hang, X. Zhang, X. Sun, C. Li, W. Liu, Q. Li, Y. Ma, *ACS Appl. Mater. Interfaces* **2018**, *10*, 24573.
- [82] Y. Zeng, X. Zhang, Y. Meng, M. Yu, J. Yi, Y. Wu, X. Lu, Y. Tong, *Adv. Mater.* **2017**, *29*, 1700274.
- [83] Z. Wang, Z. Ruan, Z. Liu, Y. Wang, Z. Tang, H. Li, M. Zhu, T. F. Hung, J. Liu, Z. Shi, C. Zhi, *J. Mater. Chem. A* **2018**, *6*, 8549.
- [84] T. Sun, Q. Nian, S. Zheng, X. Yuan, Z. Tao, *J. Power Sources* **2020**, *478*, 228758.
- [85] C. Xu, B. Li, H. Du, F. Kang, *Angew. Chem. Int. Ed.* **2012**, *51*, 933.
- [86] C. Xu, S. W. Chiang, J. Ma, F. Kang, *J. Electrochem. Soc.* **2013**, *160*, A93.
- [87] A. Huang, W. Zhou, A. Wang, M. Chen, Q. Tian, J. Chen, *J. Energy Chem.* **2021**, *54*, 475.
- [88] M. H. Alfaruqi, J. Gim, S. Kim, J. Song, P. Duong Tung, J. Jo, Z. Xiu, V. Mathew, J. Kim, *Electrochim. Commun.* **2015**, *60*, 121.
- [89] D. Xu, B. Li, C. Wei, Y.-B. He, H. Du, X. Chu, X. Qin, Q.-H. Yang, F. Kang, *Electrochim. Acta* **2014**, *133*, 254.
- [90] L. Jiang, Z. Wu, Y. Wang, W. Tian, Z. Yi, C. Cai, Y. Jiang, L. Hu, *ACS Nano* **2019**, *13*, 10376.
- [91] Q. Zhao, X. Chen, Z. Wang, L. Yang, R. Qin, J. Yang, Y. Song, S. Ding, M. Weng, W. Huang, J. Liu, W. Zhao, G. Qian, K. Yang, Y. Cui, H. Chen, F. Pan, *Small* **2019**, *15*, 1904545.
- [92] Y. Wang, Z. Wu, L. Jiang, W. Tian, C. Zhang, C. Cai, L. Hu, *Nanoscale Adv.* **2019**, *1*, 4365.
- [93] H. Ren, J. Zhao, L. Yang, Q. Liang, S. Madhavi, Q. Yan, *Nano Res.* **2019**, *12*, 1347.
- [94] T. Zhao, G. Zhang, F. Zhou, S. Zhang, C. Deng, *Small* **2018**, *14*, 1802320.
- [95] M. Shi, P. Xiao, C. Yang, Y. Sheng, B. Wang, J. Jiang, L. Zhao, C. Yan, *J. Power Sources* **2020**, *463*, 228209.
- [96] S. Kim, J. Kim, D. B. Ahn, S. Lee, *Small* **2020**, *16*, 2002837.
- [97] D. Feng, T.-N. Gao, L. Zhang, B. Guo, S. Song, Z.-A. Qiao, S. Dai, *Nano-Micro Lett.* **2020**, *12*, 14.
- [98] X.-T. Guo, J.-M. Li, X. Jin, Y.-H. Han, Y. Lin, Z.-W. Lei, S.-Y. Wang, L.-J. Qin, S.-H. Jiao, R.-G. Cao, *Nanomaterials* **2018**, *8*, 301.
- [99] Y. Fu, Q. Wei, G. Zhang, X. Wang, J. Zhang, Y. Hu, D. Wang, L. Zuin, T. Zhou, Y. Wu, S. Sun, *Adv. Energy Mater.* **2018**, *8*, 1801445.
- [100] L. Chen, Z. Yang, H. Qin, X. Zeng, J. Meng, H. Chen, *Electrochim. Acta* **2019**, *317*, 155.
- [101] H. Moon, K.-H. Ha, Y. Park, J. Lee, M.-S. Kwon, J. Lim, M.-H. Lee, D.-H. Kim, J. H. Choi, J.-H. Choi, K. T. Lee, *Adv. Sci.* **2021**, *8*, 2003714.
- [102] X. Wu, Y. Xiang, Q. Peng, X. Wu, Y. Li, F. Tang, R. Song, Z. Liu, Z. He, X. Wu, *J. Mater. Chem. A* **2017**, *5*, 17990.
- [103] X. Zhang, J. Li, H. Ao, D. Liu, L. Shi, C. Wang, Y. Zhu, Y. Qian, *Energy Storage Mater.* **2020**, *30*, 337.
- [104] C. Liu, Q. Li, H. Sun, Z. Wang, W. Gong, S. Cong, Y. Yao, Z. Zhao, *J. Mater. Chem. A* **2020**, *8*, 24031.
- [105] L. Chen, Z. Yang, F. Cui, J. Meng, Y. Jiang, J. Long, X. Zeng, *Mater. Chem. Front.* **2020**, *4*, 213.
- [106] L. Chen, Z. Yang, H. Qin, X. Zeng, J. Meng, *J. Power Sources* **2019**, *425*, 162.
- [107] B. Wu, G. Zhang, M. Yan, T. Xiong, P. He, L. He, X. Xu, L. Mai, *Small* **2018**, *14*, 1703850.
- [108] Y. Liu, X. Zhou, R. Liu, X. Li, Y. Bai, H. Xiao, Y. Wang, G. Yuan, *ACS Appl. Mater. Interfaces* **2019**, *11*, 19191.
- [109] X. Zang, X. Wang, H. Liu, X. Ma, W. Wang, J. Ji, J. Chen, R. Li, M. Xue, *ACS Appl. Mater. Interfaces* **2020**, *12*, 9347.
- [110] J. Huang, X. Tang, K. Liu, G. Fang, Z. He, Z. Li, *Mater. Today* **2020**, *17*, 100475.
- [111] J. Mao, F. F. Wu, W.-H. Shi, W.-X. Liu, X.-L. Xu, G.-F. Cai, Y.-W. Li, X.-H. Cao, *Chin. J. Polym. Sci.* **2020**, *38*, 514.
- [112] J. Zhang, Y. Huang, Z. Li, C. Gao, S. Jin, S. Zhang, X. Wang, H. Zhou, *Nanotechnology* **2020**, *31*, 375401.
- [113] X. Zhu, Z. Cao, W. Wang, H. Li, J. Dong, S. Gao, D. Xu, L. Li, J. Shen, M. Ye, *ACS Nano* **2021**, *15*, 2971.
- [114] S. Luo, L. Xie, F. Han, W. Wei, Y. Huang, H. Zhang, M. Zhu, O. G. Schmidt, L. Wang, *Adv. Funct. Mater.* **2019**, *29*, 1901336.
- [115] M. Shi, B. Wang, C. Chen, J. Lang, C. Yan, X. Yan, *J. Mater. Chem. A* **2020**, *8*, 24635.

- [116] K. W. Nam, H. Kim, J. H. Choi, J. W. Choi, *Energy Environ. Sci.* **2019**, *12*, 1999.
- [117] Y. Jiang, D. Ba, Y. Li, J. Liu, *Adv. Sci.* **2020**, *7*, 1902795.
- [118] X.-Z. Zhai, J. Qu, S.-M. Hao, Y.-Q. Jing, W. Chang, J. Wang, W. Li, Y. Abdelkrim, H. Yuan, Z.-Z. Yu, *Nano-Micro Lett.* **2020**, *12*, 56.
- [119] S. Guo, S. Liang, B. Zhang, G. Fang, D. Ma, J. Zhou, *ACS Nano* **2019**, *13*, 13456.
- [120] T. Sun, Q. Nian, S. Zheng, J. Shi, Z. Tao, *Small* **2020**, *16*, 2000597.
- [121] Y. Zhang, S. Deng, G. Pan, H. Zhang, B. Liu, X.-L. Wang, X. Zheng, Q. Liu, X. Wang, X. Xia, J. Tu, *Small Methods* **2020**, 1900828.
- [122] J. Huang, Z. Wang, M. Hou, X. Dong, Y. Liu, Y. Wang, Y. Xia, *Nat. Commun.* **2018**, *9*, 1.
- [123] Y. Zhang, L. Tao, C. Xie, D. Wang, Y. Zou, R. Chen, Y. Wang, C. Jia, S. Wang, *Adv. Mater.* **2020**, *32*, 1905923.
- [124] J. Xie, X. Yang, Y. Xie, *Nanoscale* **2020**, *12*, 4283.
- [125] W. Xu, C. Sun, K. Zhao, X. Cheng, S. Rawal, Y. Xu, Y. Wang, *Energy Storage Mater.* **2019**, *16*, 527.
- [126] T. Xiong, Z. G. Yu, H. Wu, Y. Du, Q. Xie, J. Chen, Y.-W. Zhang, S. J. Pennycook, W. S. V. Lee, J. Xue, *Adv. Energy Mater.* **2019**, *9*, 1803815.
- [127] Q. Tan, X. Li, B. Zhang, X. Chen, Y. Tian, H. Wan, L. Zhang, L. Miao, C. Wang, Y. Gan, J. Jiang, Y. Wang, H. Wang, *Adv. Energy Mater.* **2020**, *10*, 2001050.
- [128] G. Fang, C. Zhu, M. Chen, J. Zhou, B. Tang, X. Cao, X. Zheng, A. Pan, S. Liang, *Adv. Funct. Mater.* **2019**, *29*, 1808375.
- [129] H. Zhang, J. Wang, Q. Liu, W. He, Z. Lai, X. Zhang, M. Yu, Y. Tong, X. Lu, *Energy Storage Mater.* **2019**, *21*, 154.
- [130] F. Lu, Q. Chen, S. Geng, M. Allix, H. Wu, Q. Huang, X. Kuang, *J. Mater. Chem. A* **2018**, *6*, 24232.
- [131] C. Sun, X. Tang, Z. Yin, D. Liu, Y.-J. Wang, G. Yang, A. Ignaszak, J. Zhang, *Nano Energy* **2020**, *68*, 104376.
- [132] L. Luo, K. Zhou, R. Lian, Y. Lu, Y. Zhen, J. Wang, S. Mathur, Z. Hong, *Nano Energy* **2020**, *72*, 104716.
- [133] T. Koketsu, J. Ma, B. J. Morgan, M. Body, C. Legein, P. Goddard, O. J. Borkiewicz, P. Strasser, D. Dambournet, *Energy Storage Mater.* **2020**, *25*, 154.
- [134] C. Zhu, G. Fang, S. Liang, Z. Chen, Z. Wang, J. Ma, H. Wang, B. Tang, X. Zheng, J. Zhou, *Energy Storage Mater.* **2020**, *24*, 394.
- [135] N. Zhang, F. Cheng, Y. Liu, Q. Zhao, K. Lei, C. Chen, X. Liu, J. Chen, *J. Am. Chem. Soc.* **2016**, *138*, 12894.
- [136] D. Zhang, J. Cao, X. Zhang, N. Insin, S. Wang, J. Han, Y. Zhao, J. Qin, Y. Huang, *Adv. Funct. Mater.* **2021**, *2009412*.
- [137] J. Ji, H. Wan, B. Zhang, C. Wang, Y. Gan, Q. Tan, N. Wang, J. Yao, Z. Zheng, P. Liang, J. Zhang, H. Wang, L. Tao, Y. Wang, D. Chao, H. Wang, *Adv. Energy Mater.* **2021**, *11*, 2003203.
- [138] Y. Tao, Z. Li, L. Tang, X. Pu, T. Cao, D. Cheng, Q. Xu, H. Liu, Y. Wang, Y. Xia, *Electrochim. Acta* **2020**, *331*, 135296.
- [139] H. Pan, Y. Shao, P. Yan, Y. Cheng, K.-S. Han, Z. Nie, C. Wang, J. Yang, X. Li, P. Bhattacharya, K. T. Mueller, J. Liu, *Nat. Energy* **2016**, *1*, 16039.
- [140] M. Chamoun, W. R. Brant, C.-W. Tai, G. Karlsson, D. Noreus, *Energy Storage Mater.* **2018**, *15*, 351.
- [141] W. Li, X. Gao, Z. Chen, R. Guo, G. Zou, H. Hou, W. Deng, X. Ji, J. Zhao, *Chem. Eng. J.* **2020**, *402*, 125509.
- [142] J. Wang, J.-G. Wang, H. Liu, Z. You, C. Wei, F. Kang, *J. Power Sources* **2019**, *438*, 226951.
- [143] X. Chen, W. Li, Y. Xu, Z. Zeng, H. Tian, M. Velayutham, W. Shi, W. Li, C. Wang, D. Reed, V. V. Khramtsov, X. Li, X. Liu, *Nano Energy* **2020**, *75*, 104869.

Manuscript received: October 25, 2021

Revised manuscript received: November 18, 2021

Accepted manuscript online: December 1, 2021

Version of record online: December 2, 2021